Research Paper

Axial turbine flow path design for concentrated solar power plants operating with CO_2 blends

Salma I. Salah [a],[*], Francesco Crespi [b], Martin T. White [a],[c], Antonio Muñoz [b], Andrea Paggini [d], Marco Ruggiero [d], David Sánchez [b], Abdulnaser I. Sayma [a]

[a] *Thermo-Fluids Research Centre, Department of Engineering, City, University of London, Northampton Square, London, EC1V 0HB, United Kingdom*
[b] *Department of Energy Engineering, University of Seville, Camino de los descubrimientos s/n, 41092 Seville, Spain*
[c] *Thermo-Fluid Mechanics Research Centre, School of Engineering and Informatics, University of Sussex, Brighton, BN1 9RH, United Kingdom*
[d] *Baker Hughes, Turbomachinery & Process Solutions, Baker Hughes, Via Felice Matteucci, Firenze, 50127, Italy*

ARTICLE INFO

ABSTRACT

The utilisation of certain blends based on supercritical CO_2 (sCO_2), namely $CO_2/TiCl_4$, $CO_2/C_6 F_6$ and CO_2/SO_2, have been found to be promising for enhancing the performance of power cycles for Concentrated Solar Power (CSP) applications; allowing for up to a 6% enhancement in cycle efficiency with respect to a simple recuperated CO_2 cycle, depending upon the nature of the used blend and the cycle configuration of choice. This paper presents an investigation of the impact of adopting these sCO_2-based blends on the flow path design for a multi-stage axial turbine whilst accounting for aerodynamic, mechanical and rotordynamic considerations. This includes assessing the sensitivity of the turbine design to selected working fluid and imposed optimal cycle conditions. Ultimately, this study aims to provide the first indication that a high-efficiency turbine can be achieved for a large-scale axial turbine operating with these non-conventional working fluids and producing power in excess of 120 MW. To achieve this aim, mean-line aerodynamic design is integrated with mechanical and rotordynamic constraints, specified based on industrial experience, to ensure technically feasible solutions with maximum aerodynamic efficiency. Different turbine flow path designs have been produced for three sCO_2 blends under different cycle boundary conditions. Specifically, flow paths have been obtained for optimal cycle configurations at five different molar fractions and two different turbine inlet pressure and temperature levels of 250 & 350 bar and 550 & 700 °C respectively. A total-to-total turbine efficiency in excess of 92% was achieved, which is considered promising for the future of CO_2 plants. The highest efficiencies are achieved for designs with a large number of stages, corresponding to reduced hub diameters due to the need for a fixed synchronous rotational speed. The large number of stages is contrary to existing sCO_2 turbine designs, but it is found that an increase from 4 to 14 stages can increase the efficiency by around 5%. Ultimately, based on the preliminary cost analysis results, the designs with a large number of stages were found to be financially feasible compared to the designs with a small number of stages.

1. Introduction

The performance of Concentrated Solar Power (CSP) plants is significantly affected by the thermal efficiency of the power block; where a maximum cycle efficiency of 42% can be obtained by conventional subcritical steam Rankine cycles operating at a maximum steam temperature of 540 °C [1]. Further efficiency enhancement in conventional steam cycles, by up to 4.5%, can be achieved by operating at supercritical conditions. Unfortunately, this would result in an increase in the power block capital cost [1] and in slower plant dynamics (less flexibility) during startup and shutdown. Supercritical CO_2 (sCO_2) cycles have

been proposed due to their potential to outperform traditional steam cycles for CSP applications if maximum cycle temperatures exceed approximately 550 °C [2–5]. This could bring about large reductions in the Levelised Cost of Energy (LCoE) and increase the competitiveness of CSP plants in comparison with conventional power generation systems.

The efficiency enhancement enabled by supercritical CO_2 cycles is primarily a result of reducing compression work through increasing the working fluid density throughout the compression process, alongside the subsequent positive impact on the potential for internal heat recovery. This can be enabled by either condensing the working fluid, or by

Nomenclature

Acronyms

CFD	Computational fluids dynamics
Cond.	Condenser
CSP	Concentrated Solar Power
EoS	Equation of State
ER	Expansion Ratio
HRU	Heat Rejection Unit
HTRec	High Temperature Recuperator
LCOE	Levelised Cost of Energy
LTRec	Low Temperature Recuperator
ORC	Organic Rankine cycle
PHX	Primary Heat Exchanger
PR	Pressure Ratio
Rec.	Heat Recuperator
SCARABEUS	Supercritical Carbon dioxide/Alternative fluids Blends for Efficiency Upgrade of Solar power plants
sCO_2	Supercritical Carbon Dioxide

Greek Symbols

ζ_S	Stator enthalpy loss coefficient [–]
ζ_R	Rotor enthalpy loss coefficient [–]
Δh	Enthalpy rise [kJ/kg]
η_{th}	Thermal efficiency [%]
η_{tt}	Total-to-total efficiency [%]
Λ	Degree of reaction [–]
ϕ	Flow coefficient [–]
ψ	Loading coefficient [–]
ρ	Gas density [kg/m^3]
σ	bending stress [MPa]

Roman Symbol

$\dot{m}$	Mass flow [kg/s]
c	Chord length [m]
D	Diameter [m]
h	Blade height [m]
n	number of stages/rotor blades [–]
o	Throat opening [m]
s	Blade pitch [m]
t	Trailing edge blade thickness [m]
TIT	Turbine Inlet Temperature [°C]
W_s	Specific Work [kJ/kg]
X_i	Molar fraction of dopant [%]
Y	Total pressure loss coefficient [–]

Subscripts

blades	rotor blades
hub	at the hub
in	inlet
max	maximum
opt	optimum

PHX	Primary Heat Exchanger
stage	turbine stages
compr	compressor
turb	turbine

fluid can be increased by doping sCO_2 with other fluids, hence enabling condensation at elevated temperatures of the cooling medium [3,6–8].

The European Commission funded SCARABEUS project [9] aims to demonstrate the potential of using CO_2 blends for large-scale plants in the order of 100 MW$_e$. The use of selected blends that lead to higher critical temperatures enables condensation at elevated temperatures, which would increase the conversion efficiencies of supercritical CO_2 power cycles in CSP plants to values of around 50%. Hence, the cycle efficiency can be increased by up to 6 percentage points compared to a simple recuperated CO_2 cycle depending on the cycle configuration of choice and the nature of the selected blend. In this regard, the SCARABEUS consortium has investigated several chemical compounds as possible additives to sCO_2. Amongst these, three candidate dopants have been found to be particularly interesting: Titanium Tetrachloride ($TiCl_4$, [10]), Hexafluorobenzene (C_6F_6, [11]) and Sulphur Dioxide (SO_2, [12]). Using these dopants enables thermal efficiencies higher than 50% for minimum cycle temperatures (condenser outlet) as high as 50 to 55°C and for a turbine inlet temperature of 700 °C [3]. Furthermore, this high thermal performance can be achieved with these blends using relatively simple cycle layouts, namely simple recuperated for $TiCl_4$, precompression for C_6F_6 and recompression for SO_2. These configurations do not require the addition of inter-cooling and re-heating processes; features that seem to be essential to enhance the performance of pure sCO_2 cycles for CSP applications [13] even if they also increase the system capital cost [14]. As a consequence, the use of CO_2-based blends seems to be a very promising means to simultaneously increase cycle efficiency and reduce capital costs.

Supercritical CO_2 power cycles are associated with turbomachinery of a small physical size due to the high density of the working fluid and the low-pressure ratios of the cycle. This could result in more compact turbomachinery, with lower manufacturing, installation and maintenance costs. However, given that sCO_2 turbines operate at high inlet pressures and temperatures, typically between 20 and 25 MPa [15] and 400 and 800 °C [16] respectively, they do face some design and operational challenges. Their performance is highly affected by clearance, windage and frictional losses which are typically associated with a compact turbine design, alongside the high density and low kinematic viscosity of the working fluid. The novelty of the working fluid also introduces some uncertainty regarding the suitability of existing design models. Consequently, developing accurate and robust design and performance analysis tools is an important step towards developing new designs, and several studies on this topic have been published for different turbine scales and architectures. Multiple designs have been presented for sCO_2 radial turbines with a power rating of 100–200 kW [17], 50–85 kW [18], 1.5 MW [19,20] and 10 MW [21], while other authors have focused on designing axial turbines for up to 15 MW [16,20,22,23]. Fewer studies have focused on developing designs for large-scale axial turbines with net power outputs around 100 MW power rating [24], and no studies have previously considered blends. Conceptual designs have also been developed for axial turbines with power ratings of 246 MW, 450 MW, 645 MW and turbine efficiencies of 92.9%, 90.0% and 90.0% have been predicted respectively [25–27].

To explore the feasibility and operation of the CO_2 cycle and to test key components, several test rigs have been developed, which includes the development of experimental turbine prototypes with up to 8 MW power output [28–33]. Within the group of developed prototypes, there is a single 1 MW axial turbine, whilst the rest have been of the radial

performing the compression process close to the critical point of CO_2. Nonetheless, achieving this is not feasible for CSP plants inasmuch as they are typically located in hot, arid regions lacking water- or steam-cooling resources. Alternatively, the critical temperature of the working

Table 1

Dopants thermophysical properties (columns 2 to 6) and hazard according to NFPA 704 [36] (columns 7 to 10).

Chemical Compound	MWL [kg/kmol]	T_{cr} [°C]	P_{cr} [bar]	Molecular complexity [–]	Thermal stability	Health hazard	Flammability	Chemical reactivity	Special hazard
CO_2	44.01	31.06	73.83	−9.324	>700 °C	2	0	0	Simple Asphyxiant
SO_2	64.06	157.60	78.84	−8.230	>700 °C	3	0	0	–
C_6F_6	186.06	243.58	32.73	12.740	<625 °C	1	3	0	–
$TiCl_4$	189.69	364.85	46.61	1.922	>700 °C	3	0	2	React with water

turbine configuration. It has been found that sCO_2 turbines experience several operational challenges due to the compact geometries, high density and low kinematic viscosity of the working fluid compared to air. This results in challenges related to the design of the seals and bearings, particularly for small-scale demonstrators which are associated with high rotational speed and the increased potential for rotordynamic instability. On a different note, the high inlet temperature can pose challenges related to material selection, alongside challenges related to the throttle control and turbine stop valve, since the valves are placed at the highest temperature point in the cycle [34]. Furthermore, structural and mechanical considerations have been found to be highly significant for dense working fluids such as sCO_2 [35]. Specifically, supercritical CO_2 is expected to result in higher aerodynamic loads compared to air and steam turbines, partly due to the large pressure differences experienced across the turbine, but also because of the high density of the fluid. Ultimately, these considerations can introduce constraints that reduce the feasible turbine design space; hence, it becomes important to consider structural and mechanical design aspects throughout the design process to ensure feasible turbine designs are obtained.

Previous studies have focused on the conceptual design of turbomachinery and the development of testing facilities for CO_2 based plants, with an emphasis on radial turbine configurations with a reduced power rating. Comparatively, the current study, and the SCARABEUS project more generally, is concerned with the use of sCO_2 blends within large-scale CSP plants (100 MW$_e$) that utilise an axial turbine. Given that the turbine efficiency significantly affects the overall plant performance, it is important to ensure that high efficiency axial turbine designs can be achieved for the optimal blend and cycle conditions that result in the highest cycle thermal efficiency. Therefore, the aim of this paper is to study the impact of adopting different sCO_2-based blends on the turbine flow path design, and to assess the achievable aerodynamic performance whilst accounting for practical mechanical and rotordynamic constraints. Moreover, the paper aims to assess the sensitivity of the turbine design to the working fluid selected and to the boundary conditions resulting from cycle optimisation.

The novelty of this work lies in achieving the stated aim by introducing both mechanical and rotordynamic design constraints within a mean-line aerodynamic design model to restrict the maximum bending stress acting on the blades and the axial flow path length. Ultimately, the results from this study provide the first indication that a high-efficiency turbine with an efficiency in excess of 92% can be achieved for a 100 MW$_e$ power cycle operating with sCO_2-based blends.

The paper is structured as follows: an overview of the thermodynamic cycle modelling used to define the boundary conditions for the turbine design is presented in Section 2. The turbine design methodology is summarised in Section 3, which includes details relating to the aerodynamic design process alongside the mechanical design considerations that apply for large-scale axial turbine. The results are presented and discussed in Section 4, where the effect of the selected blend and imposed cycle boundary conditions on cycle and turbine performance are evaluated (Sections 4.1 and 4.2). Finally, the main conclusions of this study are presented in Section 5.

2. Cycle modelling

In order to study the impact of adopting different sCO_2-based blends on the turbine flow path design, cycle simulations were carried out

using Thermoflex, which is a commercial software [37] selected for its widely-recognised reliability. The simulations were conducted for a wide range of possible blends with the aim of defining a set of turbine boundary conditions to be considered in the turbomachinery analysis.

Thermal efficiency (η_{th}) is taken as the main figure of merit for cycle performance, although a detailed comparison of other performance metrics based on both first and second law analyses can be found in previous publications by the authors [3,38]. Thermal efficiency is expressed as the ratio of cycle specific work W_s to the enthalpy rise across the primary heat exchanger Δh_{PHX}, where the latter is a direct indicator of the heat recovery potential of the cycle (a lower Δh_{PHX} implies a larger heat recovery internal to the cycle):

$$\eta_{th} = \frac{W_{turb} - W_{compr}}{\dot{m}_{turb}\Delta h_{PHX}} = \frac{W_s}{\Delta h_{PHX}} \tag{1}$$

Three different chemical compounds are taken into account to produce CO_2 blends, namely Hexafluorobenzene (C_6F_6), Titanium Tetrachloride ($TiCl_4$) and Sulphur Dioxide (SO_2), and their main thermophysical properties are provided in Table 1. These dopants are chosen due to their good availability and the potential performance enhancement. In particular, a preliminary screening carried out by the SCARABEUS consortium has revealed that using C_6F_6, $TiCl_4$ and SO_2 resulted in the largest enhancement in cycle performance among more than thirty chemical compounds [8,11,12]. It is worth noting that the three selected dopants present different thermodynamic behaviour, particularly in terms of critical pressure and molecular complexity.[1] However, they all have a critical temperature significantly higher than that of pure CO_2, which is a key feature required for to enable working fluid condensation at a minimum cycle temperature up to 50–60 °C. A brief overview of potential safety hazards for the three selected dopants, developed according to standard 704 of the National Fire Protection Association, is presented in Table 1. The use of both $TiCL_4$ and SO_2 might face some potential limitations because of the corrosion effects due to the high reactivity of $TiCl_4$ with air moisture and the formation of H_2SO_4 when SO_2 combines with water. This is currently being investigated by the SCARABEUS consortium (more information about the utilisation of SO_2 can be found in [12]). Despite this, it is worth highlighting that the health hazards posed by SO_2 or $TiCl_4$ are very similar to, and potentially even lower than, those of other fluids commonly employed in CSP plants, such as Therminol VP1 (a common heat transfer fluid in parabolic-trough power plants), or in air-conditioning and refrigeration systems, such as ammonia, propane and R-1234yf [12]. More information about these compounds can be found in previous publications by the authors [3,6]. Focusing on other environmental considerations, these dopants present virtually no ozone depletion or global warming potential and they are not included in the lists of ozone-depleting and green-house gases by the United States Environmental Protection Agency (EPA, [41,42]). According to EPA, very high concentrations of Sulphur Dioxide may present some issues related to the formation of acid rain [43], but two observations can be made in this regard. Firstly, high concentrations of SO_x are typically

---

[1] The molecular complexity of a fluid is directly related to the molecular structure and the degrees of freedom of the atoms in its molecule, and it can be considered proportional to the specific heat [39]. In this work, it has been estimated as $(T_c/R) \cdot (dS/dT)_{T_R=0.7}$, according to [40](p. 109).
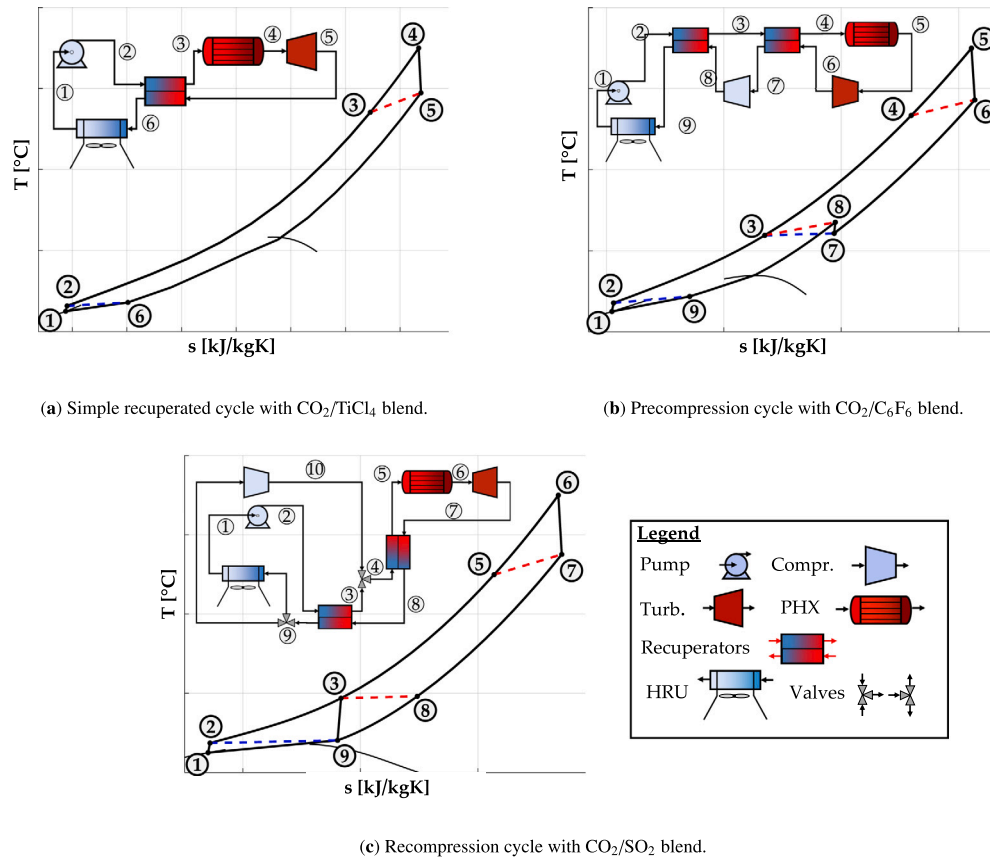
(a) Simple recuperated cycle with $CO_2/TiCl_4$ blend.

(b) Precompression cycle with CO_2/C_6F_6 blend.

(c) Recompression cycle with CO_2/SO_2 blend.

Fig. 1. Cycle layouts considered in the analysis.
Source: Adapted from [45].

produced from the exhaust/stack gases from combustion processes. However, no combustion takes place within the SCARABEUS CSP plant, and hence the only source of SO_2 released to the environment is through leakage from the system and these can be minimised in rotating machinery by the utilisation of dry gas seals [44]. Secondly, such leakages could be virtually eliminated in the near future as a result of the adoption of hermetically sealed turbomachines. Accordingly, the environmental impact of the selected dopants considered within SCARABEUS is deemed minimal.

The thermal stability of the dopants is currently being experimentally investigated within the SCARABEUS consortium. A summary of the main results is presented in Table 1. Titanium Tetrachloride ($TiCl_4$) shows very promising results, with thermal degradation observed only for temperatures above 700 °C. Currently, no detailed information is available for CO_2 and SO_2, which are currently being tested, although several references in the literature indicate that this blend is thermally stable for temperatures higher than 700 °C [46]. On the contrary, C_6F_6 has been found to show clear signs of thermal degradation for temperatures above 600 °C [47].[2] For this reason, turbine inlet temperatures exceeding this temperature are not considered for this dopant.

Previous studies have demonstrated that the selection of the best cycle layout depends strongly on the nature of the dopant employed [3]. For this reason, simple recuperated, precompression and recompression cycles are considered in this paper, for $CO_2/TiCl_4$, CO_2/C_6F_6 and CO_2/SO_2 respectively. This selection is based on earlier studies which confirmed that these configurations are capable of better exploiting the potential of each dopant. The three cycles, whose layouts are

provided in Fig. 1, are considered here in transcritical configuration due to the condensing characteristics of the proposed plant concept. A simple recuperated cycle sets a direct constraint on turbine exhaust pressure, which is constrained by the condensation pressure that is defined from the minimum cycle temperature. Even if this is not a problem for the $CO_2/TiCl_4$ blend, which is characterised by an extremely high recuperative potential, it degrades the thermal performance when using CO_2/C_6F_6 and CO_2/SO_2 blends. Thus, the precompression and recompression configurations have been considered, which are minor variations of the simple recuperated cycle that involve splitting the internal heat recovery process in two (i.e., through low and high-temperature recuperators (LTR and HTR)) and the installation of an additional compressor in the cycle.

In the recompression layout, a recompressor is added at the outlet from the low-pressure LTR to enhance heat recovery by balancing the heat capacity rate of the two streams [48]. As for the precompression cycle, a precompressor is installed in the low-pressure stream between the low and high-temperature recuperators. This helps to overcome the constraint imposed by the condensation temperature on the turbine exhaust pressure, thereby increasing the specific work of the cycle. It is worth noting that these configurations were proposed around 50 years ago by Gianfranco Angelino for power cycles running with pure CO_2 [48].

To assess the influence of dopant concentration on cycle performance and turbine design, a sensitivity analysis was carried out considering this parameter (see Table 2). This analysis aims to explain the underlying thermodynamic behaviour of each cycle configuration considered in order to identify the most promising operating conditions. To do so, the following molar fraction X_i ranges are defined for each dopant: 10%–20% for C_6F_6, 14%–24% for $TiCl_4$ and 30%–40% for SO_2. In each case, eleven different molar fractions are considered, at 1%

---

[2] This threshold temperature was obtained by the University of Brescia and Politecnico di Milano within the SCARABEUS project [47].

Table 2
Set of dopant specifications employed: range of molar fraction (X_i), Equations of state (EoS) and Binary Interaction parameter (K_{ij}).

| Dopant	X_i [%]	EoS	K_{ij}
TiCl$_4$	14–24	Standard Peng–Robinson	0.0704
C$_6$F$_6$	10–20	Standard Peng–Robinson	0.16297–0.0003951 T[K]
SO$_2$	30–40	Standard Peng–Robinson	0.0242

Table 3
Boundary conditions and specifications of turbomachinery and heat exchangers.

PIT [°C]	TIT [°C]	P_{max} [bar]	η_{is} [%] Pump/Turb/Compr	ΔT_{min} [°C]	ΔP_{heater} [bar]	ΔP_{cond} [bar]	ΔP_{rec}[%] Low P/High P
50	550/700	250	88/92/89	5	1.5	1	1/1.5
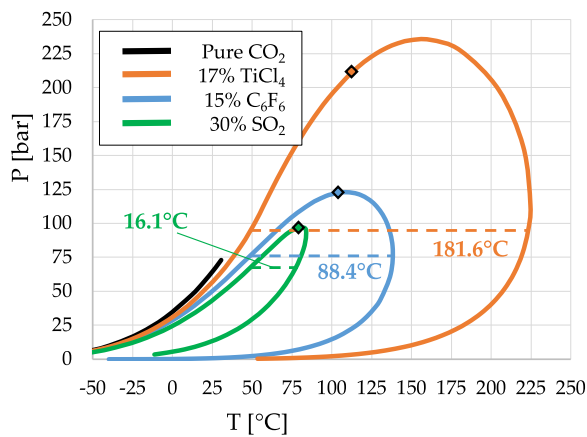
(**a**) Pressure-Temperature envelopes for different SCARABEUS blends.
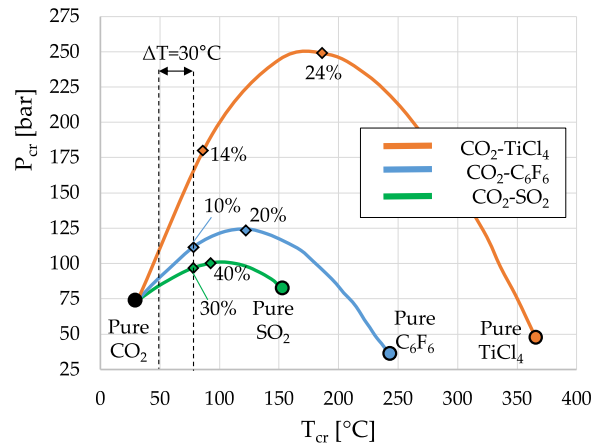
(**b**) Critical Loci of the three dopants considered.

Fig. 2. Pressure–Temperature envelopes for three different blends and pure CO$_2$ (left) and critical loci for the three dopants (right), adapted from [12]. In Figure (a), critical points are represented by markers while temperature glides for a bubble temperature of 50 °C are indicated with dotted lines and their numerical values are reported in the labels.

intervals (e.g., 10-11-12...20% for C$_6$F$_6$ case), and then a reduced number of representative cases are identified and employed as boundary conditions for the turbine analysis (the criteria used in this selection are reported in Section 4.2.1).

The molar fraction ranges are obtained starting from the lower bound (i.e., minimum allowable dopant fraction), which is strongly dependent on the nature of the chemical compound considered. The criterion used to define the lower bound for each dopant is that the difference between the minimum cycle temperature (T_{min}) and the critical temperature of the resulting blend (T_{cr}) must be equal to or higher than 30 °C. This 30 °C temperature gap is a conservative assumption made to ensure that the compression process is not carried out in close proximity to the critical point (for more information, see [12]). In the present study, T_{min} is set to 50 °C, which means that the resulting T_{cr} must be equal to or higher than 80 °C; this corresponds to a minimum dopant molar fraction of 10%, 14% and 30% for C$_6$F$_6$, TiCl$_4$ and SO$_2$ respectively. The different values are caused by the heterogeneous thermodynamic behaviour of the blends considered, which is caused by each dopant leading to a different critical point. It is worth noting that dopants with higher critical temperatures yield wider, and more pronounced, Pressure–Temperature envelopes and critical loci curves. A graphical representation of this is shown in Fig. 2, where the critical points of the three blends are presented together with an indication of the aforementioned 30 °C temperature gap and the resulting minimum dopant molar fractions considered in this study. The critical loci curves, along with the thermophysical properties of all blends, have been obtained with the standard Peng–Robinson Equation of State.[3] The

corresponding Binary Interaction Parameters (K_{ij}), provided in Table 2, have been obtained by regression of experimental VLE (Vapour Liquid Equilibrium) data available within the Aspen library [50–52].

Further information regarding the computational environment can be found in one of the authors' previous works [3]. In the current study, a common set of boundary conditions and assumptions for key system components are employed, as summarised in Table 3. A gross power output of 100 MW$_e$ is considered, while two different turbine inlet temperatures are taken into account: 550 °C to represent a state-of-the-art value for solar towers, and 700 °C, which is representative of next-generation CSP plants. Additionally, a sensitivity analysis on the maximum cycle pressure is carried out, which is varied between 250 and 350 bar.

3. Turbine design methodology

To design the turbine aerodynamic flow path, a multi-stage mean-line design approach has been implemented. The model used in the current study builds on an earlier model, and full details of the approach can be found within one of the authors' previous works [53], alongside the details provided in Appendix A. In summary, within the previous model the steady-state mass, energy, and momentum equations were solved at each station within the turbine at the turbine mean

---

[3] Recent publications by the SCARABEUS consortium identified PC-SAFT as the best Equation of State to estimate the thermo-physical properties of

CO$_2$/SO$_2$ blends under real gas conditions (close to the critical point) [12,49]. Nevertheless, the boundary conditions of the turbine in the present paper correspond to thermodynamic behaviour that is very close to that of an ideal gas, with compressibility factors ranging from 1.01 to 1.05 [12]. Bearing this in mind, the utilisation of Peng–Robinson EoS in this manuscript is not a concern in terms of accuracy.

diameter. Designing the flow path at a constant mean-diameter results in a hub diameter that decreases from the turbine inlet to the turbine exhaust, and this results in an increase in the radius ratio along the turbine. As a result, turbine blades with a larger chord size are required to limit the stresses on the blade roots, which in turn has a knock-on effect since larger chord sizes result in larger roots and introduce additional challenges relating to the stiffness and rotordyanmics of the rotor. Therefore, the previous design methodology [53], has been updated to enable the flow path to be constructed assuming a fixed hub diameter and a variable mean diameter, which reduces the impact of these potential rotordynamic and mechanical challenges. The design model assumes repeating stages, and for a given set of design inputs the blade geometry, velocity triangles and thermodynamic properties can be obtained for each turbine stage; further details on the design variables are provided later in this section. To evaluate the aerodynamic performance of the turbine, the design tool is integrated with the Aungier [54] loss model to obtain the total pressure loss coefficients for the stator and rotor of each stage. This loss model has been found by the authors to be the most suitable for sCO_2 turbine design [53]. The losses considered in the model include profile, secondary flow, tip clearance and trailing edge losses [54]. In line with the thermodynamic cycle analysis, the thermodynamic properties for the blends are obtained using the standard Peng–Robinson equation of state (EoS) using consistent binary interaction parameters.

In addition to evaluating the aerodynamic turbine performance, mechanical and rotordynamic design constraints are introduced into the mean-line design methodology. This ensures only technical feasible turbine designs are proposed, which in turn enables a fair comparison of the achievable turbine performance for the different dopants and corresponding cycle conditions (i.e., composition, pressures, temperatures and mass-flow rate). The main mechanical and rotordynamic constraints are introduced based on industrial experience and are formulated from a number of key design parameters that can be easily assessed and controlled throughout the mean-line design process. The rationale for the mechanical design can be summarised as follows:

- Synchronous designs with a rotational speed of 3,000 RPM (i.e., 50 Hz grid frequency) are selected for a plant power with a net power output of 100 MW sCO_2, due to the difficulty of incorporating a gearbox for such turbine scales.
- Considering that the expanding fluid is characterised by a large power density, it is assumed that the bending stresses generated by the expansion are more critical than the centrifugal stresses generated by blade rotation. Thus, the target in the mean-line design is to keep the static bending stresses under a suitable limit. For the preliminary design phase a limit of < 130 MPa has been set based on industrial experience considering alternating and centrifugal stresses that are consistent with sCO_2 applications.
- The bending stress limit is fixed at a constant value for all stages, regardless of the different operating temperatures encountered by each stage. This assumption is reasonable since the blade materials identified for this application are all nickel-based alloys, which do not exhibit significant degradation in the mechanical properties of interest within the operating range of the whole turbine (inlet to exhaust).
- The chords of the airfoils of each blade row are scaled targeting bending stresses within the limit established. Static stresses are calculated assuming a constant dimensionless second moment of area of the airfoil and without considering any stress intensification factor, where this factor was considered in the establishment of the bending stresses threshold.
- To allow the preliminary sizing of the blade root, and to subsequently estimate the rotor stiffness parameter, a preliminary value for the airfoil chord length is selected (< 100 mm). The rotor stiffness is an essential parameter driving the rotordynamic behaviour of the turbine.

- The number of stages and the estimation of the chord length allows an estimation of the overall length of the flow path. Longer flow path designs are associated with smaller hub diameters and since weight is proportional to the flow path length and to the hub diameter squared, it could be anticipated that increasing the number of stages may not increase cost. However, since the overall cost of the turbine is an essential criterion within the SCARABEUS project a cost analysis is included in a later section of this paper.
- The estimation of the overall length of the flow path enables a preliminary assessment of rotordynamic stability within the mean-line design with the introduction of the slenderness ratio (SR); this is defined as the ratio of the bearing span to the hub diameter. The limiting value for the slenderness ratio has been established based on the results of detailed rotordynamic assessments carried out for other similar turbines for supercritical CO_2 applications (< 9).

Within the multi-stage axial turbine design model, a constant enthalpy drop is assumed across each stage, whilst a constant value for the loading coefficient (ψ), flow coefficient (ϕ), degree of reaction (Λ), trailing edge to throat ratio (t/o) and pitch to chord ratio (s/c) of each stage is assumed. These assumed values are listed in Table 4. These parameters are set based on well established turbomachinery design practices, and whilst it is true that a further increase of turbine efficiency may be achieved through additional refinement of these parameters, one can expect the designs obtained under these assumptions to result in practically feasible designs that result in high efficiencies. More specifically, the loading and flow coefficients are selected to allow for an optimum turbine aerodynamic performance based on the Smith chart [55], while the trailing edge to throat ratio is selected to reduce the trailing edge losses based on the specified range in the literature [56]. Finally, the pitch to chord ratio is set based on recommendations within the literature [57]. The axial spacing between the turbine stages, and the radial tip clearance gap, have been specified as a percentage of the upstream pitch and tip diameter respectively.

Alongside the specified design parameters, an initial assumption for the number of rotor blades (n_{blades}), number of stages (n_{stages}), total-to-total efficiency (η_{tt}) and stator enthalpy loss coefficient (ζ_S) is specified for each case. This allows the velocity triangles and thermodynamic properties along the flow path to be obtained. Following this, the blade geometry can be obtained for each stage based on the specified pitch-to-chord ratio, which includes the chord length (c), hub diameter (D_{hub}), blade height (h) and pitch (s). Using the Aungier loss correlations, the total pressure loss coefficients are then predicted [54] and these are converted to enthalpy loss coefficients using the correlations defined in Ref. [58]. The mean-line design is then repeated using the updated values for ζ_S and the total-to-total efficiency of each stage (η_{tt}). Once the system of equations converges, the design can be evaluated based on the specified rotordynamic and mechanical constraints to ensure that $\sigma_{bending}$, c and SR are within the threshold limits. If the design does not meet the specified criteria, the number of blades (35 < n_{blades} < 100) and number of stages are adjusted manually until the mechanical and rotordynamic design constraints are met. As a general example, the chord length should be increased (and the number of blades decreased accordingly to maintain the same solidity) to reduce the bending stresses and the number of stages should be reduced to allow for a reduced slenderness ratio. A more detailed description of the design methodology is provided in Appendix A.

The turbine design model has been verified and cross-checked with published numerical and experimental studies in previous work by the authors [53]. Specifically, this covers different working fluids including air, sCO_2 and R245fa, with power rating between 144 kW and 10 MW. A good agreement is obtained for the blade dimensions and flow angles, alongside the predicted total-to-total efficiency, with maximum percentage differences of 1.3% and 1.2% in the total-to-total and total-to-static efficiency respectively within the four selected verification cases. Further details are also presented in Appendix A.
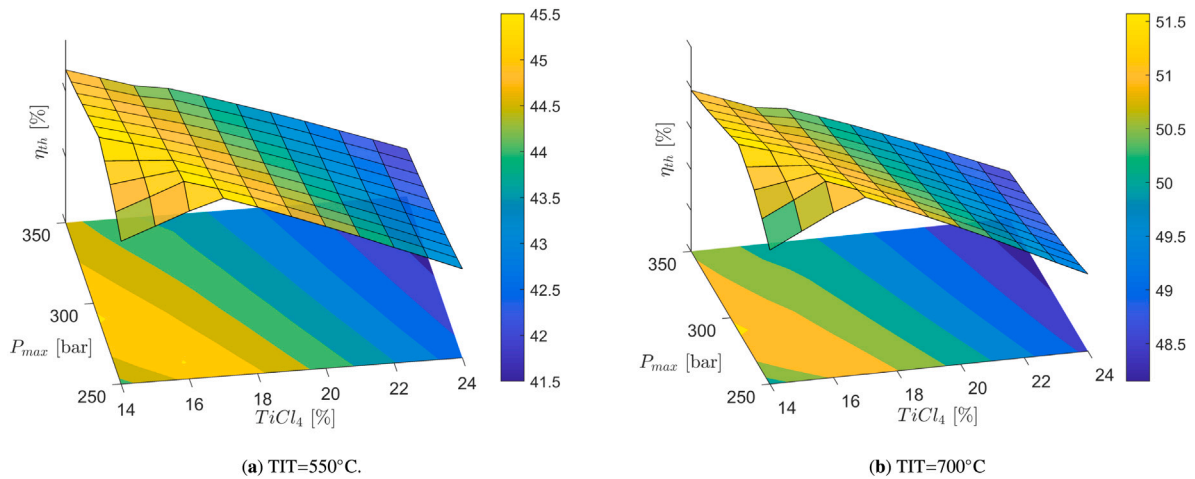
(a) TIT=550°C.

(b) TIT=700°C

Fig. 3. Thermal efficiency of a simple recuperated cycle operated with $CO_2/TiCl_4$ blend as a function of maximum cycle pressure and dopant molar fraction. Two turbines inlet temperatures are considered.

Table 4
Mean-line turbine design parameters.

Decision variables	Description	Units	Value
N	Rotational speed	[RPM]	3000 (50 Hz motor)
k_s	Surface roughness	[mm]	0.002
ϕ	Stage flow coefficient	[–]	1 [55]
ψ	Stage loading coefficient	[–]	0.5 [55]
Λ	Degree of reaction	[–]	0.5 [55]
t/o	Trailing edge thickness to throat ratio	[–]	0.05 [56]
s/c	Pitch-to-chord ratio	[–]	0.85 [57]

Fig. 4. Thermal efficiency of a precompression cycle operated with CO_2/C_6F_6 blend as a function of maximum cycle pressure and dopant molar fraction, considering a turbine inlet temperature of 550 °C (results at 700 °C are not reported due to the limited thermal stability of this blend).

4. Results and discussions

4.1. Cycle analysis

In this section, the results obtained for variable dopant concentration, maximum cycle pressure (P_{max}) and turbine inlet temperature (TIT) are discussed. This discussion is driven by the impact on thermal efficiency, with the objective to select the cases with highest efficiency for the associated turbine flow path design.

Figs. 3 to 5 present the trend of thermal efficiency (η_{th}) as a function of the molar fraction and maximum pressure for $TiCl_4$, C_6F_6 and SO_2 respectively, using a combined surface and contour map. The first important observation is that the simple recuperated cycle with $TiCl_4$ is the only cycle whose thermal efficiency is significantly affected by the variation in P_{max} and X_i. For this system, η_{th} ranges from 41.5% up to 45.5% at 550 °C TIT and from 48 to 51.5% at 700 °C. On the contrary, the thermal efficiency of the precompression cycle with C_6F_6 is barely affected by changes in maximum pressure and molar composition, with values in the range 42.75–43.15% at 550 °C. Finally, the recompression cycle with SO_2 exhibits more intermediate behaviour, with thermal efficiency in the order of 43.5–44.5% and 50.3–51.5% at 550 °C and 700 °C respectively, showing only a slight dependence on both P_{max} and X_i.

Other interesting observations can be made by focusing on the optimum molar composition (i.e. the molar fraction of dopant that yields peak cycle efficiency). For $CO_2/TiCl_4$ blend, the molar fraction varies significantly with maximum cycle pressure, from 18% at 250 bar down to 14% for 350 bar, though its dependence on TIT is very weak.
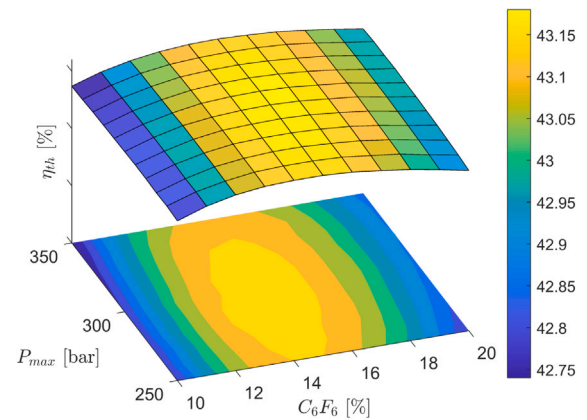
At both temperature levels (550 °C and 700 °C), peak thermal efficiency values are achieved at mid- to low molar fractions and pressures while efficiency is lowest on the top-right corner of the contour map (high P_{max} and X_i). The situation changes drastically for CO_2/SO_2 blend, which achieves optimum performance for dopant concentrations around 30%, regardless of the inlet pressure and temperature. Interestingly, considering the contour maps, the optimum P_{max} is found to depend on the temperature considered, shifting from 310 bar to 350 bar when TIT is increased from 550 °C to 700 °C. A thorough explanation of this pattern, based on a 2nd-law analysis, is provided in [45]. Nevertheless, from a practical standpoint, the interest in operating at such high pressures may be offset by the technical limitations derived from the need for bulkier, more expensive equipment, which may not be compensated for by the limited η_{th} gain. Therefore, a thorough thermo-economic analysis will be required to identify the optimum cycle operating conditions.

The dissimilar scenario for each dopant is a result of adopting different cycle layouts for the different blends. This is better understood if thermal efficiency is expressed as the ratio of cycle specific work W_s to the enthalpy rise across the primary heat exchanger Δh_{PHX}, see Equation (1). For a closed recuperative cycle, operating with a given working fluid composition, an increase in pressure ratio (PR) results in higher values of W_s & Δh_{PHX}. On the one hand, W_s is enhanced due to the higher turbine expansion ratio (ER). On the other
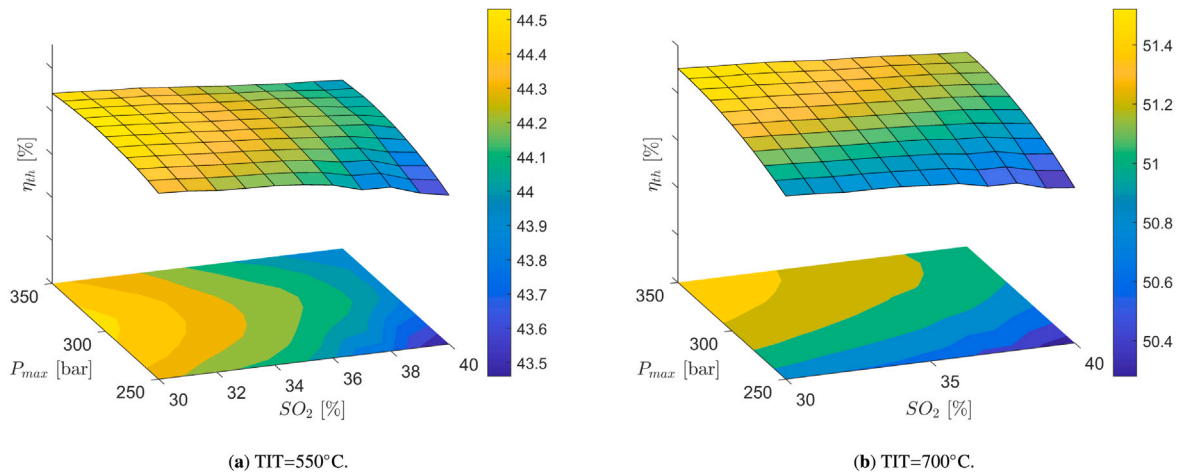
Fig. 5. Thermal efficiency of a recompression cycle operated with CO_2/SO_2 blends as a function of maximum cycle pressure and dopant molar fraction. Two turbines inlet temperatures are considered.

hand, a higher ER also leads to a lower turbine outlet temperature, which directly affects the PHX inlet, thus increasing Δh_{PHX}. The higher pressure ratios come not only from a higher P_{max} but also from the higher X_i dictated by the condensing nature of the transcritical layouts investigated in this study. In such systems, the pump inlet pressure ($P_{in,pump}$) is set by the minimum cycle temperature ($T_{min} = 50 \,°C$) and a higher concentration of dopant implies a lower pump inlet pressure, brought about by the higher critical temperature and pressure of the blend [3]. This results in higher cycle pressure ratios if a constant maximum cycle pressure is considered, and this become even more evident when P_{max} and X_i are increased at the same time. However, in this case the change in working fluid composition leads to significantly different thermodynamic properties which consequently affect the heat recovery potential; this leads to an overall drop of W_s and Δh_{PHX}, and a significant rise in the working fluid mass flow rate [3]. In both cases, the thermal efficiency of the investigated cycle is determined by the trade-off between the variations observed in specific work, and the heat recovery potential as a consequence of the higher cycle pressure ratio. Therefore, in order to understand the reasoning between the different trends of η_{th} shown in Figs. 3(a) to 5(a), a deeper analysis of the effect of varying the PR on W_s and Δh_{PHX} for each system is necessary.

For this purpose, two different scenarios are analysed: variable P_{max} for constant blend composition and variable blend composition for constant maximum cycle pressure. In the first case, the trends of the different metrics of interest, namely η_{th}, W_s, Δh_{PHX}, $\dot{m}$, $P_{in,pump}$, PR and ER, are presented in Figs. 3 to 5 as a function of P_{max} and normalised with respect to the value corresponding to the lowest P_{max} in the analysis. In the second case, the dependence of these parameters on dopant concentration for a given P_{max} is shown in Figs. 3(b) to 5(b). This analysis has only been carried out for a turbine inlet temperature of 550 °C to limit the length of this section. In fact, a similar scenario would be observed considering 700 °C TIT, although it would be characterised by lower variations in Δh_{PHX}. This is due to the fact that a higher TIT enables higher turbine exhaust temperatures, thus offsetting the aforementioned effect brought by an increase in the cycle pressure ratio. This clarifies the reason behind the results presented in Figs. 3 to 5 at 700 °C; they are very similar to those obtained at 550 °C but shifted towards higher pressures.

Fig. 6(a) shows that thermal efficiency peaks at a P_{max} of around 290 bar for a simple recuperated cycle with $86\%CO_2/14\%TiCl_4$. Increasing the pressure to 350 bar results in a smaller difference between the normalised W_s and Δh_{PHX} and this brings about a lower η_{th}. It is observed that pump inlet pressure remains constant since constant values for both T_{min} and X_i are considered. This does not apply to Fig. 6(b) (P_{max} set to 250 bar), where a progressive reduction in

$P_{in,pump}$, and an increase in $\dot{m}$, are observed due to the higher dopant concentration. These changes bring about a lower relative increase in PR than that observed in Fig. 6(a) due to the significantly lower drop in $P_{in,pump}$ compared to the rise in P_{max}. This has an impact on thermal efficiency which increases initially, then peaks when the molar fraction of $TiCl_4$ reaches 17% and finally experiences a clear drop. Once again, this can be explained by the relative variations of Δh_{PHX} and W_s; while the latter decreases almost linearly with X_i, Δh_{PHX} shows a significant drop initially, followed by an evolution that is less steep. From these results, it becomes clear that the efficiency of the simple recuperated cycle is strongly dependent on maximum pressure and dopant concentration. This is due to the recuperated cycle layout not having any additional degree of freedom to balance the effect of sub-optimal values of these parameters.

Contrary to the simple recuperated case, the two advanced layouts considered, namely precompression and recompression, introduce additional degrees of freedom. As discussed in Section 2, the former layout is characterised by an additional compressor in the low pressure section that is installed in-between the two heat recuperators. This component helps to overcome the constraint set by the minimum cycle temperature on turbine exhaust pressure, hence allowing turbine expansion ratio to be optimised to yield benefits in terms of W_s (see increasing trends of ER_{Turb} and W_s in Fig. 7(a). Fig. 7(a) shows the variation of P_{max} for a precompression cycle operating with $85\%CO_2/15\%C_6F_6$. As presented in Fig. 7(a), the relative variation of ER is significantly different from that of PR, yielding fairly similar variations of W_s and Δh_{PHX} and subsequently a fairly constant trend for thermal efficiency. On the other hand, the slight increase in η_{th} observed in Fig. 7(b) with dopant concentration corresponds to a lower relative reduction in W_s than in Δh_{PHX}, brought about by an increasing turbine expansion ratio.

The recompression cycle does not aim to significantly increase specific work, but rather to improve the regenerative potential of the cycle in order to increase efficiency. To this end, the amount of working fluid circulating through the high-pressure/low-temperature side of LTR is reduced. Ultimately, this helps to balance the heat capacity rates of the two streams in this heat exchanger, thus reducing the irreversibility of the heat transfer process and increasing thermal efficiency. This is observed by comparing the results in Figs. 6(a) to 8(a), which applies to a recompression cycle running with $70\%CO_2/30\%SO_2$. In the latter plot, the relative growth of Δh_{PHX} and W_s is very similar and yields almost constant thermal efficiency with a very weak dependence on P_{max}. Similarly, the slight reduction in η_{th}, observed in Fig. 8(b), is a result of the very similar relative deviations experienced by Δh_{PHX} and W_s, which is in turn brought about by the opposing effects of the split-flow factor and $P_{in,Pump}$.

(**a**) Variable P_{max}, constant $TiCl_4$ concentration (14%(v)).

(**b**) Variable dopant concentration, constant P_{max} (250 bar).
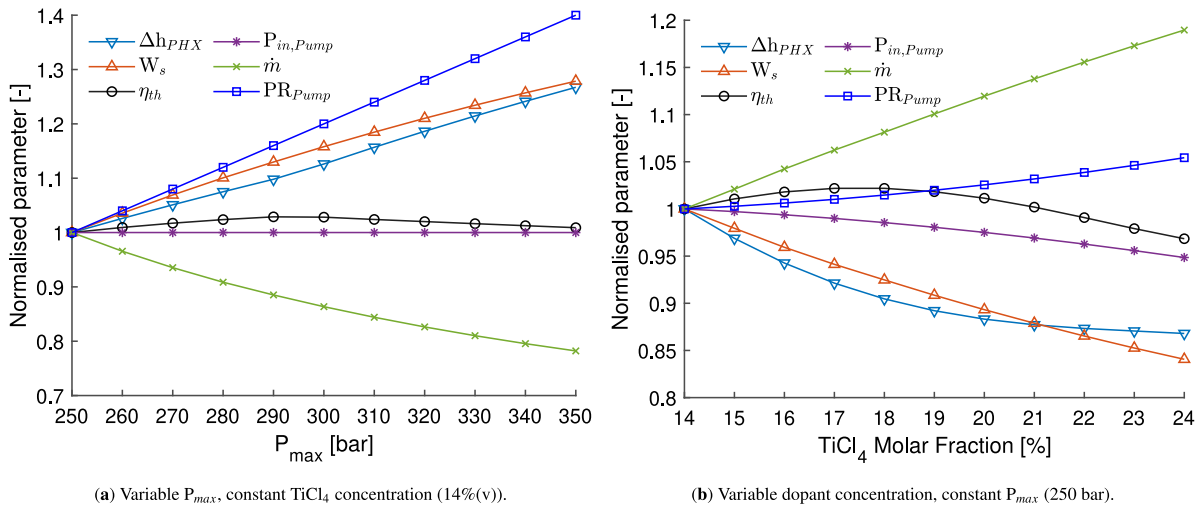
Fig. 6. Relative variation of various cycle parameters as a function of maximum pressure and dopant concentration. A simple recuperated cycle operating on $CO_2/TiCl_4$ blends is considered. Turbine Expansion ratio is not plotted since it is equivalent to pump Pressure Ratio.

(**a**) Variable P_{max}, constant concentration of C_6F_6 (15%(v)).

(**b**) Variable dopant molar fraction, constant P_{max} (250 bar).

Fig. 7. Relative variation of various cycle parameters as a function of maximum pressure and dopant concentration. A precompression cycle operated with CO_2/C_6F_6 is considered.

(**a**) Variable P_{max}, constant concentration of SO_2 (30%(v)).

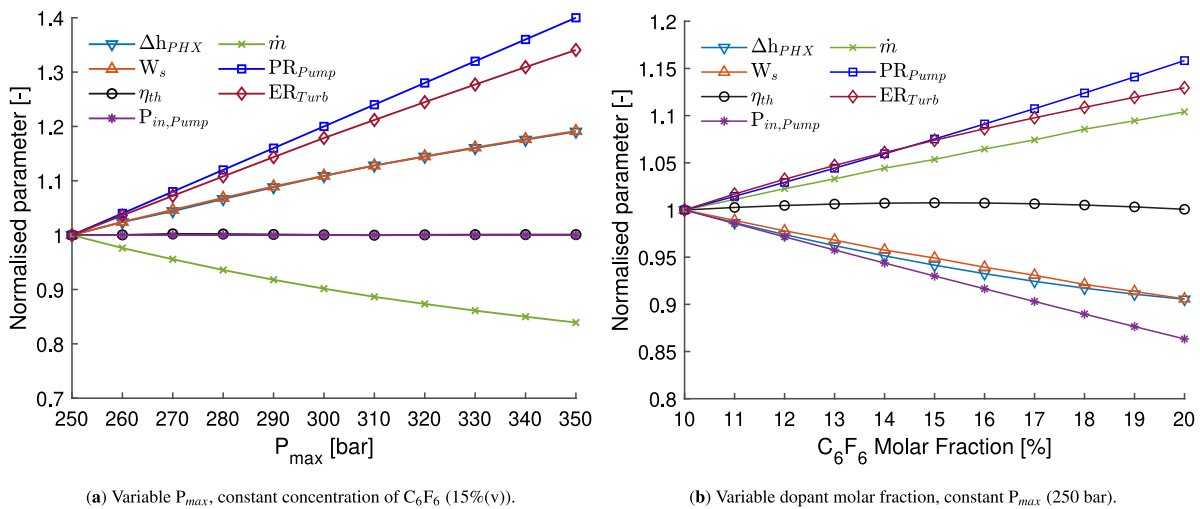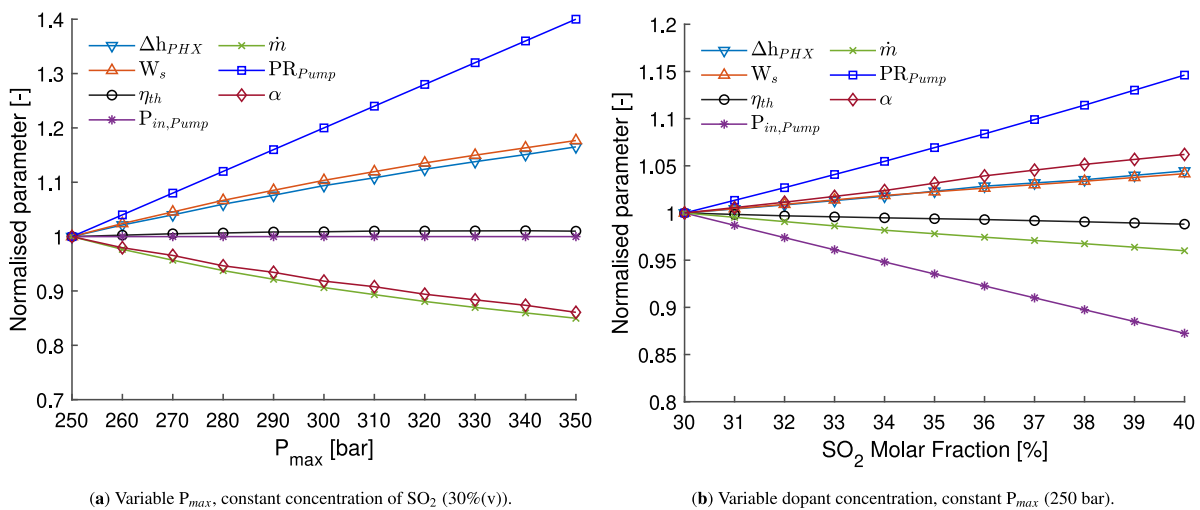(**b**) Variable dopant concentration, constant P_{max} (250 bar).

Fig. 8. Relative variation of various cycle parameters as a function of maximum pressure and dopant concentration. A recompression cycle running on CO_2/SO_2 is considered. Turbine Expansion ratio is not plotted since this is equivalent to pump Pressure Ratio.

The behaviour of the cycles is strongly dependent on the thermodynamic characteristics of the blends. Blends of $CO_2/TiCl_4$, for instance, are characterised by a very wide PT-envelope (i.e., a large temperature glide, see Fig. 2(a)), which is linked to a significant difference between the critical conditions of the two constituent compounds. A positive consequence of this is that working fluid condensation starts inside the recuperator and is not limited to the heat rejection unit (HRU). Hence, this is the main reason for the extraordinary heat recovery potential of this system [3]. On the negative side, this prevents the adoption of layouts incorporating split-flow options such as the recompression cycles, and limits the beneficial effects brought by precompression [3]. On the contrary, CO_2/SO_2 blends are characterised by very narrow PT envelopes, corresponding to low temperature glides, and this avoids condensation of the working fluid within the recuperator. As a result of this, these blends perform very poorly in a simple recuperated cycle but they are particularly suitable for the recompression layout. In this regard, it is worth noting that the (limited) drop in η_{th} observed in the bottom-right corner of Fig. 5 is brought about by a significant increase in the temperature glide of the CO_2/SO_2 blend, caused by the extremely high X_i, which prevents the efficient operation of the split-flow feature. In such circumstances, the split-flow ratio is forced to take sub-optimal values to shift the inlet to the compressor away from the two-phase region (see the change in slope of the split-flow ratio trend in Fig. 8(b) for X_i higher than 35%), which leads to a lower thermal efficiency of the cycle.

4.2. Turbine design and analysis

4.2.1. Definition of candidate boundary conditions

Once the optimum working fluid composition and maximum cycle pressure levels are identified for each blend, a series of representative boundary conditions are defined to study their impact on turbine design. Firstly, the optimum P_{max} for each blend is selected, according to the results shown in Figs. 3 to 5. This corresponds to 300 bar for C_6F_6 (550 °C case only) and 310 and 350 bar for SO_2, for 550 °C and 700 °C respectively; for $TiCl_4$, 290 bar is considered regardless of TIT. Secondly, five different values of molar fraction are defined for each dopant, including the optimum and minimum/maximum values. The five molar fractions are defined for both 250 bar and optimum P_{max}, and this is done for both 550 °C and 700 °C TIT (with the exception of C_6F_6, for which only 550 °C is considered).

A dual approach is adopted to select the five molar fractions. If the optimal molar fraction X_i of dopant (i.e., the one achieving maximum η_{th}) falls between the minimum and maximum values, the remaining two cases (for a total of five sets of boundary conditions for turbine design) are selected as the arithmetic mean between the minimum and optimum values and between the optimum and maximum values respectively. For example, this is the case for a simple recuperated cycle operating with $CO_2/TiCl_4$ at TIT = 550 °C, for which the optimum X_i is 17%, and this falls within the allowable range of 14% to 24%; in this case, the other two points considered are 15.5% and 20.5% (see Table B.9).

If, on the other hand, the optimum molar fraction coincides with the minimum value, the other three points result from evenly distributing the entire range of molar fractions. This is the case of the recompression cycle operating with a CO_2/SO_2 blend, whose optimum X_i is 30%. In this case, the cases selected for turbine design are 30%, 32.5%, 35%, 37.5% and 40% (see Tables B.9 and B.10). It is worth noting that some of these molar fraction values were not considered in the previous section, where X_i took integer values only.

In summary, a set of sixty different cases are thus identified, and successively employed as input data for the turbine design process. The detailed set of specifications, along with turbine inlet and outlet conditions, can be found in Appendix B. The set is divided into four cases defined by means of different combinations of turbine inlet temperature and maximum cycle pressure. *Case A* refers to 550 °C and 250 bar, *Case*

B to 700 °C and 250 bar, *Case C* to 550 °C and the optimum P_{max} (which depends on the system considered) and *Case D* to 700 °C and optimum P_{max}.

As a final comment, it is worth remarking that, even if the present paper focuses specifically on the turbine design, the thermal performance of precompression and recompression cycles strongly depends on the efficiency of the compressor included in such configurations. The design of this equipment, which requires further investigation due to the high novelty of the working fluid employed, will be undertaken and disclosed in future work.

4.2.2. Exploration of the design space for the three candidate blends

Using the results from Section 4.2.1 the achievable turbine performance has been initially evaluated at a turbine inlet temperature and pressure of 550 °C and 250 bar respectively, and at the minimum molar fraction for the three blends (14%, 10% and 30% for $CO_2/TiCL_4$, CO_2/C_6F_6 and CO_2/SO_2 respectively). These conditions were selected to allow an initial exploration of the design space, before then conducting further investigations into the sensitivity of the turbine performance to increasing the pressure, temperature and molar fraction. Table 5 summarises the cycle conditions for the three candidate blends considering a gross power output of 100 MW_e and the assumptions specified in Table 3.

In this section, a comparison of the performance of the flow path designs obtained for each blend is presented. Initially, four stage turbine designs were selected for the three candidate blends to limit the blade peripheral speed to 180 m/s with the assumption of a constant enthalpy drop across each stage. A summary of the designs, including details of the 1st and last stages of the 4-stage flow path is presented in Table 6 for the three candidate blends.

Owing to the different thermodynamic properties of the candidate dopants, and also variations in the chosen cycle configuration, different values for the turbine stage specific work were obtained for each blend composition. As a result, large differences in the hub diameters and bending stresses were obtained. The 70%CO_2/30%SO_2 blend results in the largest hub diameter and the smallest gas bending stress as shown in Fig. 9. On the contrary, the smallest hub diameter and the highest bending stresses are attributed to the 86%CO_2/14%$TiCl_4$ blend. For the $CO_2/TiCl_4$ flow path the blade count has been lowered to keep the bending stresses within the specified limit. Increasing the blade count for this flow path would result in bending stresses exceeding the 130 MPa static bending stress limit; also the same logic applies for the CO_2/C_6F_6 and CO_2/SO_2 designs. Concerning the aerodynamic performance, the turbine design for $CO_2/TiCl_4$ achieves the highest efficiency compared to either the CO_2/C_6F_6 and CO_2/SO_2 designs, which is due to larger aspect ratio blades, smaller hub diameters and a smaller radial tip clearance gap. All three blends resulted in a slenderness ratio that is well within the specified design limit which indicates rotordynamic instability is of no concern. This also indicates there is scope to increase the flow path length, with the goal of increasing the number of stages and increasing efficiency.

To enable a fairer comparison between the three flow path designs, the effect of increasing the number of stages within the range of 4 to 14 stages was investigated for the three design cases. In the following set of results, the turbine performance is investigated based on the operating conditions specified in Table 5, which corresponds to the minimum molar fraction value for each blend. The analysis aims at examining the effect of a reduced hub diameter (D_{hub}), which is the result of increasing the number of design stages (n_{stages}), on the gas bending stress on the rotor blades ($\sigma_{bending}$), the isentropic efficiency (η_{tt}), and the slenderness ratio (SR). In this set of results, the designs are modified for each design case to keep the gas bending stress with the threshold limit, with the rotor blade count ranging between 35 and 95. Given that the highest rotor bending stresses are experienced by the last turbine stage, which is due to the combination of a reduced density, enlarged flow area and increased blade heights, the bending

Table 5
Boundary conditions for the three candidate blends at 550 °C.

Blend	X_i [%]	$\dot{m}$ (kg/s)	P_{out} (MPa)	PR (–)	η_{th} (%)	Cycle configuration
$CO_2/TiCl_4$	14	1485	9.8	2.47	44.4	Recuperated
CO_2/C_6F_6	10	1098	6.5	3.69	42.8	Precompression
CO_2/SO_2	30	1016	6.9	3.42	44.3	Recompression

Table 6
Flow path design details for the CO_2 blends for a fixed number of stages.

Parameter	$CO_2/TiCl_4$		CO_2/C_6F_6		CO_2/SO_2	
	1st stage	last stage	1st stage	last stage	1st stage	last stage
Number of stages [–]	4		4		4	
Hub diameter [mm]	876.2		1115.8		1145.5	
Bending stress [MPa]	126.9	126.7	88.4	129.3	77.7	128.0
Number of rotor blades	63	52	95	86	95	95
Radial tip clearance [mm]	0.67	0.71	0.81	0.86	0.83	0.87
Aspect ratio [–]	0.70	0.95	0.50	0.99	0.48	0.97
Slenderness ratio [–]	4.16	4.16	3.03	3.03	2.93	2.93
Total-to-total efficiency [%]	91.5		89.6		89.3	
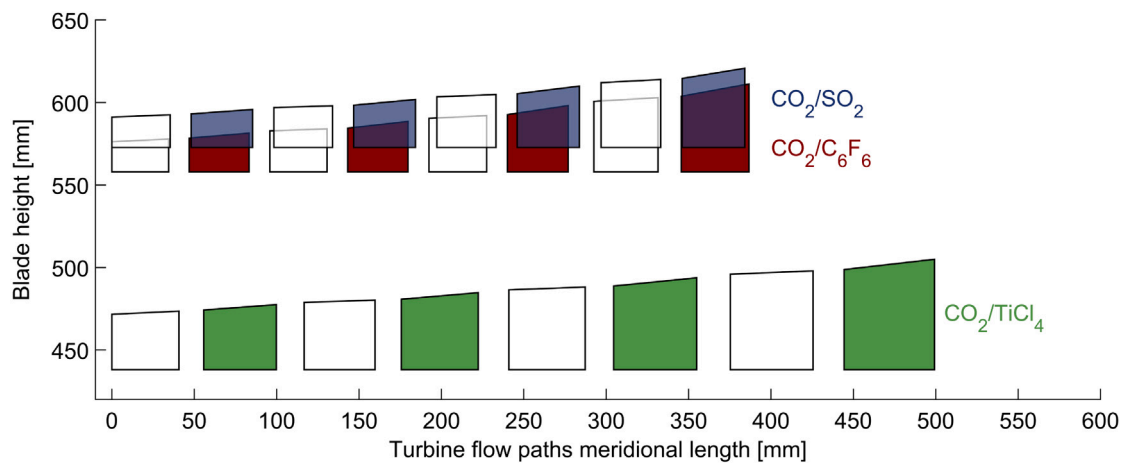
Fig. 9. Turbine flow path meridional view for four-stage turbine designs for $CO_2/TiCL_4$, CO_2/C_6F_6 and CO_2/SO_2 blends; unfilled and filled shapes represent the stator and rotor blades respectively.

stress values presented correspond to this specific stage. The results are summarised in Figs. 10(a) to 10(d).

In view of the implemented design hypothesis, within which the designs are obtained at a constant rotational speed of 3000 RPM and loading coefficient of 1, the number of stages dictates that both the blade peripheral speed and the hub diameter, and this is a function of the specific isentropic enthalpy drop for a given blend and set of operating conditions. The smallest hub diameter is achieved for $CO_2/TiCl_4$ and the largest for CO_2/SO_2. Increasing the number of stages to 14 increases the overall total-to-total efficiency to 95.6% and 94.2% for $CO_2/TiCl_4$ and CO_2/SO_2 respectively. This is compared to initial respective efficiencies of 91.5% and 89.3% for the four-stage design. This increase in the number of stages is associated with a reduction in the hub diameter and the blade peripheral speed, which results in higher efficiency due to reducing the secondary flow losses. The reduction in the blade peripheral speed enables to produce designs with longer blade heights and hence, this results in smaller chord length to blade height ratio and reduced secondary flow losses. Furthermore, less tip clearance losses are experienced with the long flow path designs as a results of the reduced the clearance gap size which is defined as a constant ratio of the tip diameter.

Increasing the number of stages also results in a higher slenderness ratio for all three-flow path designs, with the highest ratio obtained for the $CO_2/TiCl_4$ case. Moreover, to enhance the aerodynamic efficiency whilst achieving a design that complies with the rotor bending stress limit, it is necessary reduce the number of blades within the range

of 95 to 35, as shown in Fig. 11. Reducing the number of rotor blades results in a larger blade pitch, leads to longer chord lengths and smaller bending stress (both tangential and axial) on the blades. For the $CO_2/TiCl_4$ flow path, increasing the number of stages above six, whilst, at the same time, reducing the number of blades to 35 (the lower limit) results in bending stress that are above the threshold limit of 130 MPa. Therefore, the $CO_2/TiCl_4$ design should be limited to six stages in order to meet the constraints imposed on the slenderness ratio and bending stress. However, for both CO_2/C_6F_6 and CO_2/SO_2, the number of stages can be increased up to 12 stages without exceeding the maximum rotor bending stress of 130 MPa. Moreover, the slenderness ratio can be kept below 9 and the number of blades is above or equal to the minimum value of 35.

Based on the results presented in this subsection, it is possible to select the optimal number of stages, and hence hub diameter, that obtains the highest efficiency for a specified set of turbine boundary conditions. This number of stages provided the higher aerodynamic efficiency, whilst keeping the rotor bending stresses and slenderness ratio within the specified threshold limit. However, it should be noted that each pair of blend and boundary conditions results in an optimal flow path design with a different number of stages and a different number of rotor blades.

4.2.3. Sensitivity of efficiency to cycle conditions

The previous analysis was completed at the minimum blend fraction (X_1) and at an inlet temperature and pressure of 550 °C and
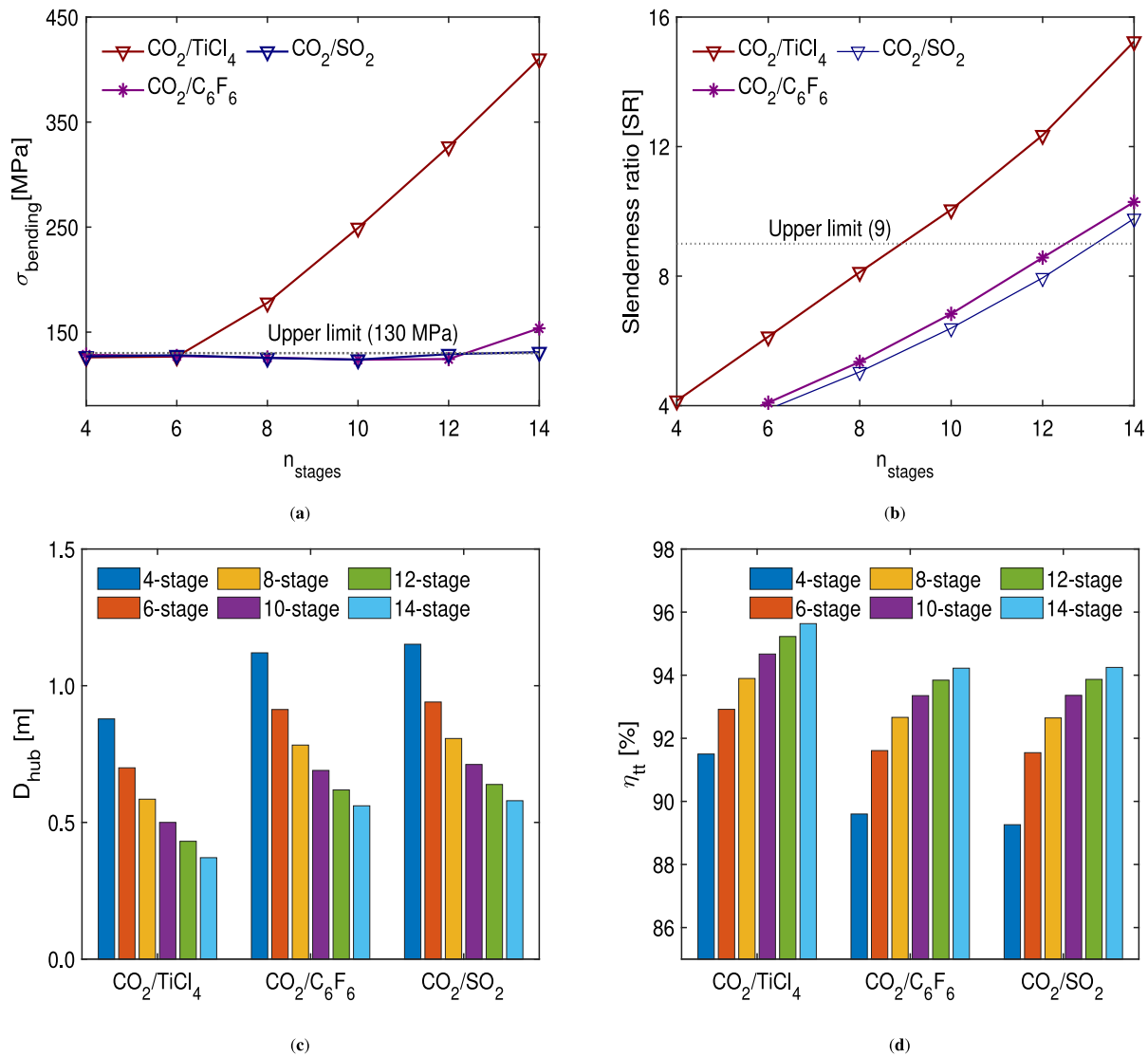
Fig. 10. Number of stages [n_{stages}] versus (a) rotor bending stress [$\sigma_{bending}$] for the last turbine stage; (b) slenderness ratio [SR] for CO_2/ $TiCl_4$, CO_2/C_6F_6 and CO_2/SO_2 blends; (c) hub diameter [D_{hub}]; (d) total-to-total efficiency [η_{tt}] for $CO_2/TiCl_4$, CO_2/C_6F_6 and CO_2/SO_2 working blends and between 4 and 14 turbine stages.

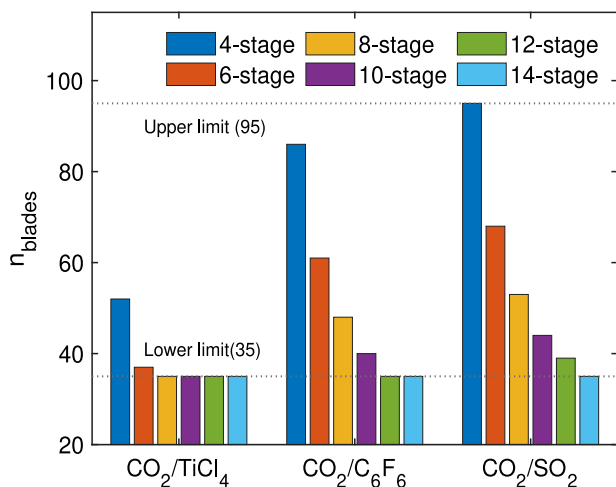**Fig. 11.** Number of rotor blades for the last turbine stage [n_{blades}] of turbines design for $CO_2/TiCl_4$, CO_2/C_6F_6 and CO_2/SO_2 with 4–14 turbine stages.

250 bar respectively. This section aims to investigate the effect of changing the thermodynamic boundary conditions, namely the turbine inlet temperature (T_{inlet}) and pressure (P_{inlet}) and dopant concentration (X_i) on the achievable turbine efficiency for a turbine design that meets the imposed mechanical and rotordynamic constraints. To do this, the remaining turbine design boundary conditions, namely the mass flow rate ($\dot{m}$), pressure ratio (PR) and molar fractions are taken from the results obtained from the thermodynamic cycle analysis. In the following set of results, as reported in Figs. 12(a) to 12(c), axial turbine designs are produced at a total inlet temperature and pressure of 550 °C & 250 bar (*Case A*), 700 °C & 250 bar (*Case B*), 550 °C & P_{opt} (*Case C*) and 700 °C & P_{opt} (*Case D*). This is completed at different molar fractions ranging from 14 to 24%, 10 to 20%, and 30 to 40% for $CO_2/TiCl_4$, CO_2/C_6F_6 and CO_2/SO_2 respectively.

For the $CO_2/TiCl_4$ blend, changing the boundary conditions of turbine design by increasing the inlet temperature from 550 to 700 °C results in a lower rotor bending stresses, and allows for a larger number of stages, smaller hub diameters and higher turbine efficiencies, whilst keeping the slenderness ratio within the defined limit as indicated in Fig. 12(a). On the other hand, less significant effects are obtained when turbine inlet pressure is increased from 25 MPa to P_{opt} for the same inlet temperature. As for the effect of molar fraction, increasing this
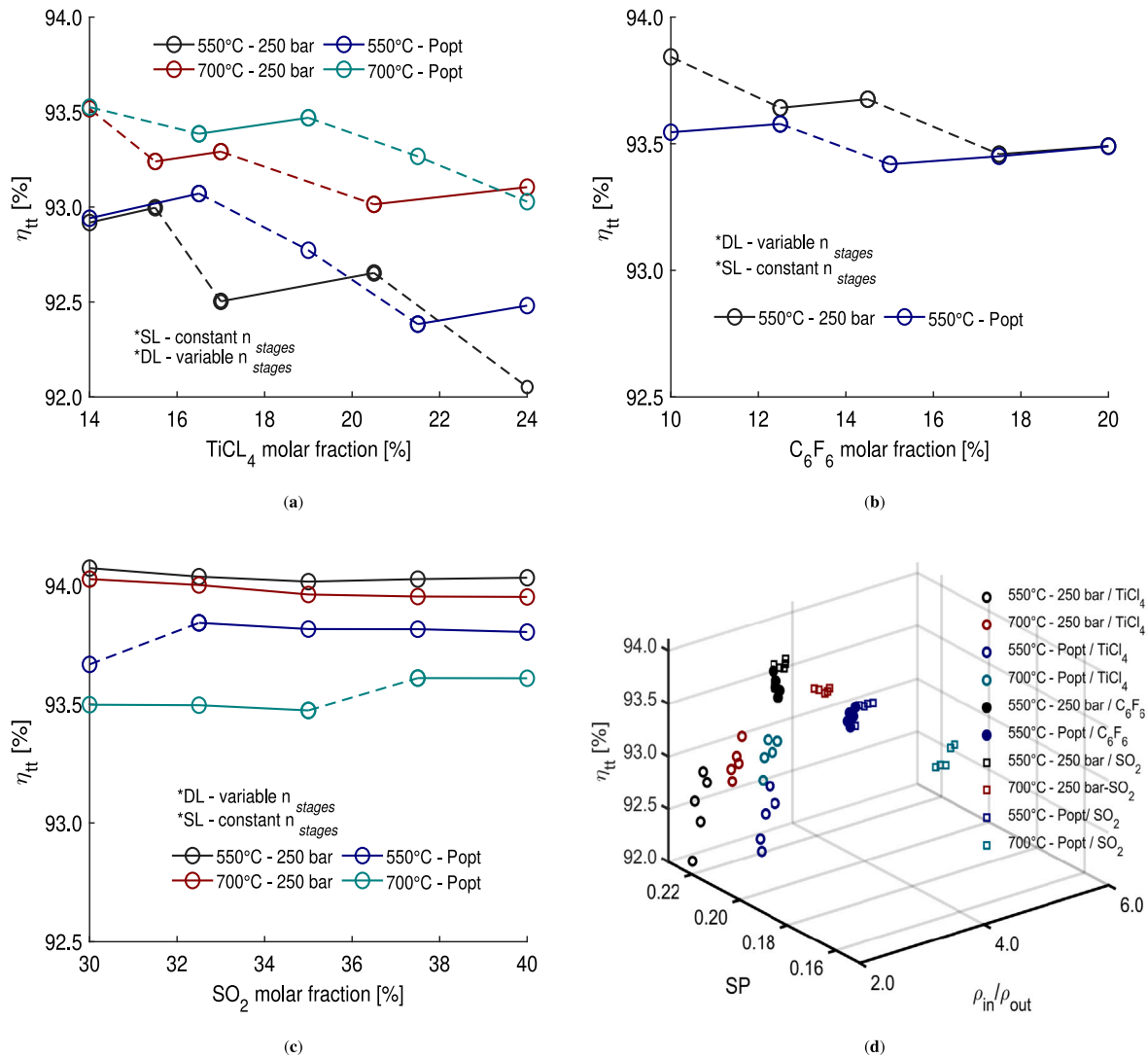
Fig. 12. Total-to-total efficiency (η_{tt}) versus dopant concentration for (a) $CO_2/TiCl_4$, (b) CO_2/C_6F_6, and (c) CO_2/SO_2.**P_{opt}: is the optimum maximum pressure for each cycle.

from 14 to 24% results in a lower turbine efficiency (η_{tt}), which is due to the increased bending stresses; hence to keep $\sigma_{bending}$ within the specified limit, the stage number should be reduced or the number of blades should be reduced and the blade chord length increased. Increasing the dopant concentration results in a lower enthalpy drop across the turbine stage and thus a larger mass flow rate is needed to produce the same plant power output. This means that larger tangential stresses are applied on the rotor blades. Nevertheless, if increasing the dopant concentration $[X_i]$ allowed for producing designs with the same number of stages, a higher total-to-total efficiency would be achieved as experienced with $X_1 \& X_2$ and $X_3 \& X_4$ at 550 °C & 250 bar (*Case A*). The feasibility of these designs is not addressed in this paper inasmuch as assessing the mechanical integrity of the flow path requires a more detailed analysis which is beyond the criteria identified for screening purposes at the mean-line design stage. It is worth highlighting that the discontinuity experienced in the turbine efficiency with respect to the molar fraction is the result of integer decision variables, namely the number of stages and number of blades, which must be adjusted in order to comply with the specified mechanical and rotordynamic limits. For example, for the 550 °C and 250 bar case with $CO_2/TiCl_4$, the number of stages is equal to 6 for a molar fraction of 14 and 15.5%, but as the molar fraction is increased to 17 and 20.5% the number of stages must be decreased to 5 to comply with the imposed constraints.

For the CO_2/SO_2 flow paths, increasing the inlet temperature from 550 to 700 °C has a less significant effect on turbine efficiency and

results in trends that are contradictory to those observed for $CO_2/TiCl_4$. Specifically, a small increase in efficiency is obtained for the low pressure case compared to the reduction in efficiency for the P_{opt} case. Increasing the inlet temperature for the CO_2/SO_2 blend results in a lower slenderness ratio for the same number of stages, and allows for a larger number of stages (Fig. 12(c)). However, as discussed in the previous section, the CO_2/SO_2 flow path design allows for a larger number of stages than the $CO_2/TiCl_4$ case, and as a result increasing the number of stages further, beyond a certain limit, results in a less significant efficiency enhancement. This is due to the small change in hub diameters that results from increasing the number of stages, which is due to the small change in blade peripheral speed that is experienced.

To analyse the effect of increasing the temperature from 550 to 700 °C, and setting turbine inlet pressure to P_{opt} for the CO_2/SO_2 flow paths, the turbine size parameter and volumetric expansion ratio are introduced. This is done to highlight the effect of the working fluid properties, cycle parameters and turbine size on the achievable turbine efficiency. The turbine size parameter is defined as $SP = \sqrt{\dot{V}_{out}}/\Delta H_s^{0.25}$, where ΔH_s is the isentropic enthalpy drop and $\dot{V}_{out}$ is the volumetric flow rate at the outlet. The volumetric expansion ratio is defined as (ρ_{in}/ρ_{out}), where ρ_{in} and ρ_{out} are the fluid densities at the turbine inlet and outlet respectively. For the low pressure cases of all blends, the resulting size parameters obtained are rather similar, although there are some differences in the volumetric expansion
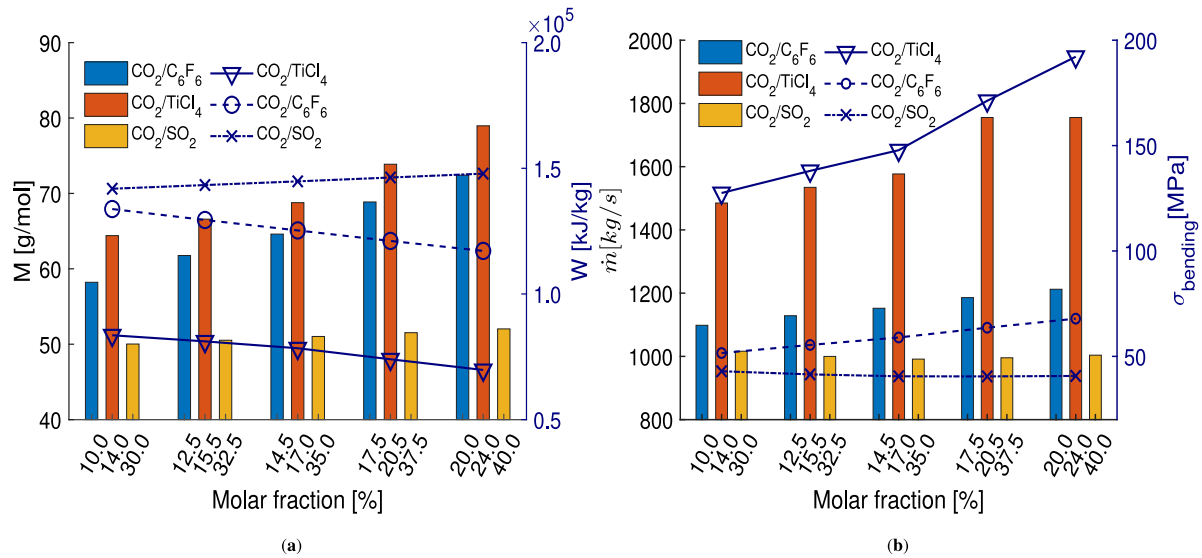
Fig. 13. Molar fraction of dopant (X_i) versus (a) molecular weight (M) and specific work (W), (b) mass flow rate ($\dot{m}$) and rotor bending stresses ($\sigma_{bending}$) with the same number of stages.

ratio. Contrary to the $CO_2/TiCl_4$ case, increasing inlet temperature for the high-pressure case results in lower turbine efficiencies for the CO_2/SO_2 flow paths due to the significant reduction in turbine size parameter (SP), alongside the increase in volumetric expansion ratio, as indicated in Fig. 12(d). For the two blends examined, a maximum absolute efficiency difference of 0.88% is obtained due to changing the molar fraction in the $CO_2/TiCl_4$ flow path at 700 °C and 250 bar. This confirms that high efficiency turbines can be designed within the SCARABEUS project for the three candidate working blends over the range of boundary conditions examined.

In the cycle optimisation, the optimum dopant concentration was found to be 17, 14.5 and 30% for the 550 °C and 250 bar inlet condition (*Case A*), for the $CO_2/TiCl_4$, CO_2/C_6F_6 and CO_2/SO_2 blends respectively. These values changed to 17 and 30% for 700 °C and 250 bar (*Case B*) operating with $CO_2/TiCl_4$ and CO_2/SO_2 blends respectively. However, the turbine mean-line design indicates that optimal turbine efficiency is obtained at different molar fractions and this corresponds to 15.5, 10, 30% for *Case A*, and 14 and 30% for *Case B* for the same blends. Consequently, it can be observed that different optimum molar fractions are obtained from the perspective of cycle performance and turbine performance. For example, for the $CO_2/TiCl_4$ case, designing the turbine at the optimum cycle molar fraction results in an absolute turbine efficiency drop of 0.52% and 0.23% compared to the optimum cycle design point for *Cases A and B*, respectively. On the other hand, if the optimum cycle thermal efficiency is compared against the one calculated with the molar fraction that maximises the turbine efficiency, a drop of 0.5 and 1.05 percentage points is observed for *Cases A and B*, respectively. A similar analysis for CO_2/C_6F_6 yields an absolute drop of 0.16% in the turbine efficiency for *Case A*; the corresponding drop in cycle efficiency is 0.36 percentage points. Ideally, the optimal molar fraction should be identified through a coupled cycle-turbine design activity, whereby the cycle and turbine are simultaneously optimised. However, due to the complexity of the turbine design process, which includes multiple-stages and the need to manually iterate integer design variables to bring the turbine design within the imposed mechanical and rotordynamics, such an approach has not been adopted; such an approach could be explored in future research. Nonetheless, it is worth remembering that this behaviour exists. However, for the purposes of this current study, it is considered most suitable to design the turbine for the optimal molar fraction that maximises the thermal efficiency of the cycle.

Regarding turbine performance, the CO_2/SO_2 flow path designs achieve the highest efficiencies at an inlet temperature and pressure

of 550 °C and 250 bar and 700 °C and 250 bar respectively. Similarly, the CO_2/C_6F_6 flow path designs achieve the highest efficiencies at an inlet temperature and pressure of 550 °C and 250 bar. However, the $CO_2/TiCl_4$ flow path achieved the highest total-to-total efficiency (η_{tt}) at an inlet temperature and pressure of 700 °C and P_{opt}. It is evident that increasing the inlet pressure for the CO_2/SO_2 blend at an inlet temperature of 700 °C results in a smaller size parameter compared to the $CO_2/TiCl_4$ case. Therefore, the $CO_2/TiCl_4$ flow path is the best performing for the 700 °C and P_{opt} case compared to the other flow paths, as indicated in Figs. 12(d).

To further elaborate on the performance of the axial turbines operating with the different candidate blends, the change in specific work, blend molecular weight, bending stresses and mass-flow rate are presented in Figs. 13(a) and 13(b) at the five different molar fractions. These figure are obtained at a turbine inlet temperature and pressure of 550 °C and 250 bar respectively (*Case A*). For the $CO_2/TiCl_4$ case, increasing the molar fraction of dopant (X_i) results in smaller hub diameters, taller blades and higher bending stress for the same number of stages (Fig. 13(b)). This confirms the more significant reduction in the number of stages experienced by the $CO_2/TiCl_4$ case with the increasing concentration of dopant, compared to both CO_2/C_6F_6 and CO_2/SO_2. This is attributed to the significant increase in the mass-flow rate required to achieve the same net power output from the plant, which is due to the lower specific work of the $CO_2/TiCl_4$ blend compared to CO_2/C_6F_6 and CO_2/SO_2. The relative increase in mass flow rate with dopant concentration is much larger for TiCl$_4$ than for the other dopants, as indicated in Figs. 6, 7 and 8(b). Although increasing the molar fraction of dopant, and hence the molecular weight of the blend, results in a lower specific work for CO_2/C_6F_6 and $CO_2/TiCl_4$, a slight increase is experienced in the CO_2/SO_2 case. Consequently, increasing the molar fraction results in designs with a lower number of stages for the $CO_2/TiCl_4$ and CO_2/C_6F_6 flow paths, which is necessary to allow for rotor bending stress and slenderness ratio within the specified limits; as a result more discontinuities are observed in the efficiency trends as shown in Figs. 12(a) and 12(b). However, for the CO_2/SO_2 case, increasing the molar fraction results in turbine designs with a larger number of stages, which is due to the larger enthalpy with increasing dopant concentrations, as indicated in Fig. 13(a). This effect has been discussed in detail in a previous work by some of the current authors [6].
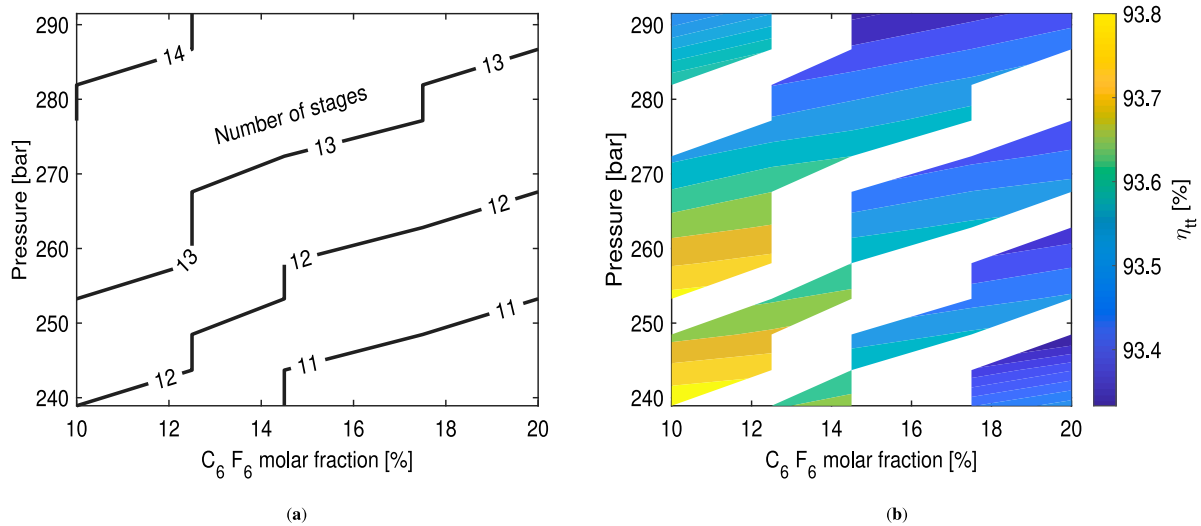
Fig. 14. Contours of the optimal (a) number of stages contours, (b) and total-to-total efficiency [%] for CO_2/C_6F_6 flow paths at a turbine inlet temperature of 550 °C at different turbine inlet pressures and dopant concentrations. Results are generated assuming a 100 MW$_e$ power plant.

4.2.4. Efficiency trends for the most technically feasible cycle

According to the health and environmental considerations discussed in Section 2, alongside the current state-of-the-art in CSP power cycles, a precompression cycle operating with CO_2/C_6F_6 at 550 °C could be considered to be the one of the most technically feasible cycles. The analysis in this subsection focuses on this cycle in more detail, and aims to examine how the achievable turbine efficiency is influenced by the target inlet pressure and blend composition.

The contours of the optimal number of stages and the corresponding turbine isentropic efficiency are reported in Figs. 14(a) and 14(b) for dopant concentrations ranging between 10 and 20% and turbine inlet pressures ranging between 240 and 300 bar. For the same molar fraction, increasing the inlet pressure results in a larger number of stages, and a lower turbine efficiency due to the increased pressure ratio and reduced mass flow rate. Similarly, for a fixed number of stages, increasing the molar fraction of dopant results in a lower turbine isentropic efficiency, where a molar fraction of 10% is found to yield highest overall turbine isentropic efficiency. Thus, for the CO_2/C_6F_6 blend, an increase in both the molar fraction and turbine inlet pressure results in a maximum drop in turbine efficiency of 0.4 points. Nonetheless, these results confirm that for the range of operating conditions considered, it is still possible to design a turbine flow path that can achieve a high isentropic efficiency.

4.2.5. Remarks about the turbine design for CO_2 blends

In summary, for the sCO$_2$ blends considered, a total-to-total turbine isentropic efficiency above 92% can be achieved. This is considered an important milestone within the SCARABEUS project, and is a promising result for developing the technology further. Moreover, it is worth reiterating that, in comparison with the reference cycle design, where an overall turbine efficiency was assumed to be equivalent to 92%, better cycle performance can be obtained for the updated flow path efficiency. On this point it should however be noted that the current study is concerned with providing an assessment for the flow path performance and does not account for the additional losses experienced with the turbine, such as inlet, bearing, balancing drum, and throttle and discharge losses that would further reduce the turbine efficiency below the results obtained here. Having said this, it is worth noting that most of these losses scale with the same parameters that influence turbine efficiency; for example, balancing drum and bearing losses are expected to be higher with larger hub diameters. On the contrary, throttle losses can be safely assumed to be low regardless of the specific flow path designs given that the size of the valves is typically chosen

targeting fluid velocities that yield similar losses. Nevertheless, these losses will have to be quantified in later design stages.

In this study, fixed values for the turbine design parameters were assumed. Thus, whilst flow path efficiencies above 92% were obtained, further enhancement in turbine performance may be possible through an extension of the optimisation process to account for the optimisation of aerodynamic design variables including pitch-to-chord ratio (s/c), flow coefficient (ϕ), loading coefficient (ψ) and degree of reaction (Λ). Optimisation for those parameters may result in further variations in the turbine design. In this regard, an additional analysis has been carried out by the authors to investigate the effect of changing these design parameters on the aerodynamic turbine performance and the flow path design. This work is on-going, but the main conclusions will be summarised here. Specifically, a parametric study was carried out for the CO_2/C_6F_6 blend operating within a precompression cycle at a inlet temperature of 550 °C. Changing both the loading and flow coefficients was found to have the most significant effect on the flow path designs compared to the other design parameters (Λ and s/c). Increasing the loading coefficient over the range from 0.8 to 1.5, at a fixed flow coefficient, pitch-to-chord ratio and degree of reaction of 0.5, 0.85 and 0.5 respectively, resulted in a reduction in the number stages from fourteen to five stages to keep the bending stresses within the threshold limit (130 MPa). This lead to a reduction in efficiency of around 4 percentage points over the examined loading coefficient range. On the contrary, increasing the flow coefficient, at a fixed loading coefficient, pitch-to-chord ratio and degree of reaction of 1.0, 0.85 and 0.5 respectively, resulted in lower bending stresses. An efficiency enhancement by up to 2.0 percentage points was obtained as a result of increasing the flow coefficient (ϕ) from 0.3 to 0.7; where the number of stages increased from six to thirteen stages. Changing the degree of reaction and pitch-to-chord ratio was found to have less significant effects on the flow path design and performance compared to both the flow and loading coefficients. Ultimately, changing the loading and flow coefficients simultaneously resulted in a maximum efficiency of 93.8%, which was obtained at values of ψ & ϕ of 0.8 and 0.6 respectively. This allows for an efficiency enhancement of 0.2% compared to the base-line design where fifteen design stages are required compared to eleven stages for the baseline design case. It is worth mentioning that the 0.2% increase in the turbine efficiency is considered within the margin of accuracy of mean-line flow path design and this indicates that there is not much benefit in modifying key turbine design parameters to improve the turbine efficiency.

It is evident that high turbine efficiency is achieved for designs that are able to accommodate a large number of stages; for example

10 to 12 stages can be accommodated for the CO_2/C_6F_6 flow path design at 550 °C and 250 bar over a molar fraction range from 10 to 20%. However, it is also important to consider the effect that increased number of stages may have on the cost of the turbine. This is another essential criterion for the development of sCO_2 power blocks for CSP plants technologies, and a particular objective of the SCARABEUS project.

In practice, the overall cost of the turbine is driven by its overall size, which is a function of the turbine diameter and of the axial length. Whilst increasing the number of stages results in a larger axial length, it also results in a smaller hub diameter. Noting that weights of the major components, such as rotor and casing, are proportional to the length, but proportional to the hub diameter squared, it may be anticipated that a turbine designed for a smaller hub diameter and a larger axial length could be cheaper compared to a turbine designed for a larger hub diameter and a smaller axial length (low number of stages). This hypothesis is aligned with common industry experience (e.g., steam turbines) if similar classes of materials are employed for the major components; in this case, the tacit equivalence between weights and costs is a reasonable assumption. However, if the major components adopt different materials whose cost per kilogram is extremely different, which is the case for nickel based alloys compared to conventional steels, the assumption may not hold.

In this regard, a preliminary direct material cost analysis has been carried out for different flow path designs to compare the cost associated with machines with a small number of stages to machines with large number of stages. The cost analysis was carried out for turbine designs produced with different number of stages over the range from 4 to 14 stages for the CO_2/SO_2 blend. The analysis was developed based on industrial experience and the methodology is presented in authors previous work [59] but the main conclusions will be summarised here. Several assumptions were made within the preliminary cost analysis methodology to allow for easily evaluating the flow path cost using the mean-line design outputs. In brief, only the direct material cost was considered in this analysis and the overall cost of the machines with a small number of stages was estimated with respect to the cost of a 14-stage $80\%CO_2/20\%SO_2$ flow path (a reference case) [60]. Fig. 15 reports the calculated cost of a range of designs with respect to the fourteen-stage case. The highest cost difference for all machines, with respect to the reference case, is due to the contribution from the inner casing; which accounts for almost 65% of the total $\Delta cost$ for the 4-stage design. This analysis indicates that the 14-stage design results in savings of almost 1.8 M€ with respect to the 4-stage machine. Examining Fig. 15 further indicates that as the number of stages increases, the cost difference compared to the reference 14-stage design reduces. Specifically, designing the turbine with more than 8-stages results in a direct material cost that only differs by around 0.1 M€ compared to the reference design. This is due to the similar radial dimensions of the machines (i.e., hub diameter) rather than the increase in the axial dimension obtained for the 14-stage design. Nonetheless, this increase in the direct material cost is considered insignificant bearing in mind that cost pricing is set based on a conservative estimates; where in reality some of the used nickel based alloys are expected to cost higher than the assumed values.

The preliminary direct material cost analysis indicated that machines with a large number of stages are financially feasible compared to the machines with a small number of stages. Although it is worth noting that the operating expenditure (OPEX) should be added to the overall machine cost to quantify the effect of efficiency differences of the machine over the lifespan of the entire plant. In this regard, the four-stage machine results in a total-to-total efficiency (η_{tt}) that is almost 6% less than the 14-stage machine, and assuming the same thermal input into the cycle, would reduce power output by around 9 MW. By considering the operating expenditure (OPEX) for all machines, the machines with less number of stages, and a lower η_{tt}, are expected to result in higher OPEX compared to the machines with a larger number of stages.
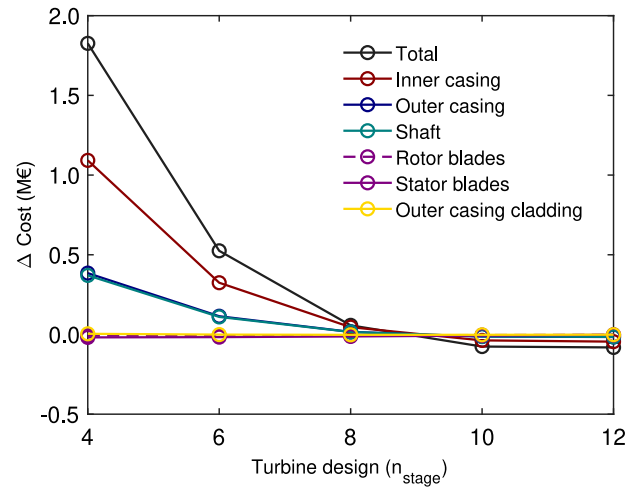

Fig. 15. Direct material cost differences associated with the different turbine designs with respect to the CO_2/SO_2 14-stage design [59].

5. Conclusions

Mean-line flow path designs for a large-scale axial turbine, for installation in a 100 MW_e CSP plant, were presented for different blends based on carbon dioxide, namely $CO_2/TiCl_4$, CO_2/C_6F_6 and CO_2/SO_2, and for different boundary conditions. The mean-line aerodynamic design was integrated with mechanical and rotordynamic constraints to limit the maximum stress acting on the blades and the length of the shaft for rotordynamic stability. The design tool was verified against case-studies from the literature for air, sCO_2 and organic Rankine cycle (ORC) turbines to ensure the suitability of the design tool for different working fluids. A maximum percentage difference of 1.5% and 1.2% in the total-to-total and total-to-static efficiency, respectively, was observed.

To study the impact of adopting different sCO_2-based blends on the turbine flow path design, multiple flow path designs were produced for different cycle operating conditions, where different turbine inlet temperatures, turbine inlet pressures and molar fractions were considered. The turbine flow paths were designed with the goal of achieving maximum aerodynamic efficiency, while meeting imposed mechanical and rotordynamic considerations. Designs with a large number of stages were found to result in higher turbine efficiencies; this corresponds to designs with reduced hub diameters due to keeping a fixed synchronous rotational speed. These designs were found to be financially feasible compared to short flow path designs based on a preliminary cost analysis. Among the examined blends, it was found that using the $CO_2/TiCl_4$ blend resulted in the shortest flow-path length compared to both CO_2/C_6F_6 and CO_2/SO_2. Furthermore, for the three CO_2 blends investigated it was possible to obtain a flow path with an overall total-to-total efficiency in excess of 92%. This is considered promising for the future of CO_2 plants. This proves that using CO_2 blends can result in high efficiencies across the range of the boundary conditions and molar fractions considered. Hence, a high component efficiency is achievable, which will help realise the thermodynamic potential of the proposed cycle designs.

Finally, the sensitivity of the turbine design to the three blends was assessed for optimised cycle conditions. This was completed for different turbine inlet pressure and temperature levels, ranging between 250 & 350 bar and defined at 550 & 700 °C respectively, and for five different molar fractions for each blend. Despite each blend showing a different level of sensitivity to the inlet temperature, pressure and molar fraction, all the flow path designs obtained were found to achieve a high aerodynamic efficiency, which is in excess of 92%, whilst meeting the rotordynamic and mechanical constraints. Moreover, a
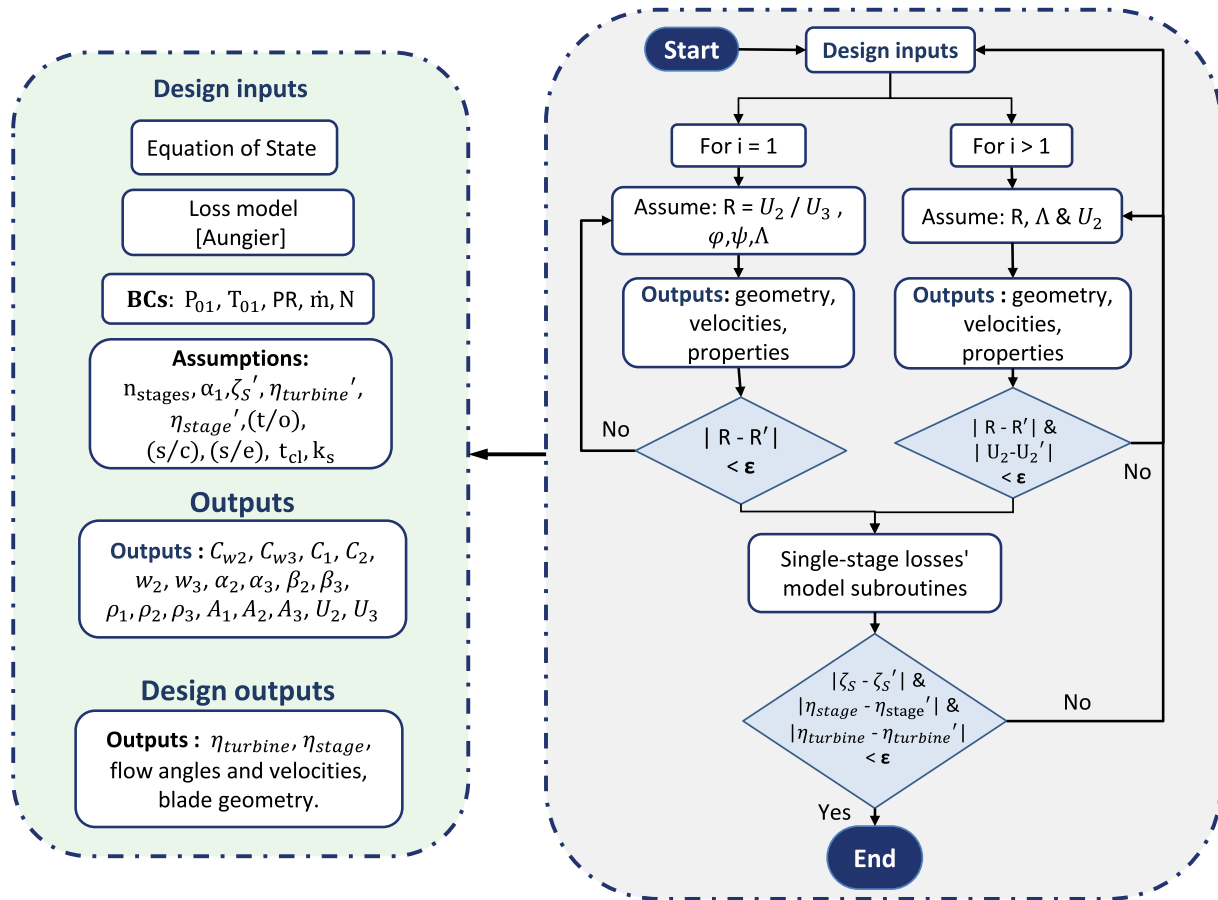
Fig. A.16. Flow chart of a multi-stage axial turbine design methodology at constant hub diameter.

cycle efficiency greater than 50% was achieved for all the investigated blends at an inlet temperature of 700 °C. Ultimately, it is concluded that designing the turbine for the optimal molar fraction that maximises the thermal efficiency of the cycle is a worthwhile endeavour.

Declaration of competing interest

The authors declare that they have no known competing financial interests or personal relationships that could have appeared to influence the work reported in this paper.

Data availability

No data was used for the research described in the article.

Appendix A. Turbine design methodology

A full description of the turbine design methodology is presented in this section, although the method largely builds on the authors previous work [53]. An iterative design process is implemented to obtain the turbine design at a constant hub diameter. The design process starts with assuming a constant enthalpy drop across the stage ($\Delta h_0 stage$), loading coefficient (ψ) of the first design stage, flow coefficient (ϕ) and degree of reaction (Λ). Based on this, the peripheral blade speed at the

rotor inlet and the axial flow velocity through the whole machine are obtained:

$$U = \sqrt{\frac{\Delta h_{0(stage)}}{\psi}} \tag{A.1}$$

$$C_a = U_2 \times \Phi \tag{A.2}$$

The relation between total enthalpy and static enthalpy at the rotor inlet and exit and the degree of reaction definition can be expressed as:

$$h_{02} = h_2 + \frac{1}{2}C_2{}^2 \tag{A.3}$$

$$h_{03} = h_3 + \frac{1}{2}C_3{}^2 \tag{A.4}$$

$$\Lambda = \frac{h_2 - h_3}{h_{01} - h_{03}} \tag{A.5}$$

The absolute velocity components C_2 and C_3 are expressed as a function of the axial (C_a) and tangential velocity components (C_w) as:

$$C_2 = \sqrt{C_a{}^2 + C_{w2}{}^2} \tag{A.6}$$

$$C_3 = \sqrt{C_a{}^2 + C_{w3}{}^2} \tag{A.7}$$

The ratio between the inlet blade speed and outlet blade speed (R) is assumed to be equal to U_2/U_3. Using Equations (A.3)–(A.5), the degree of reaction can be expressed as:

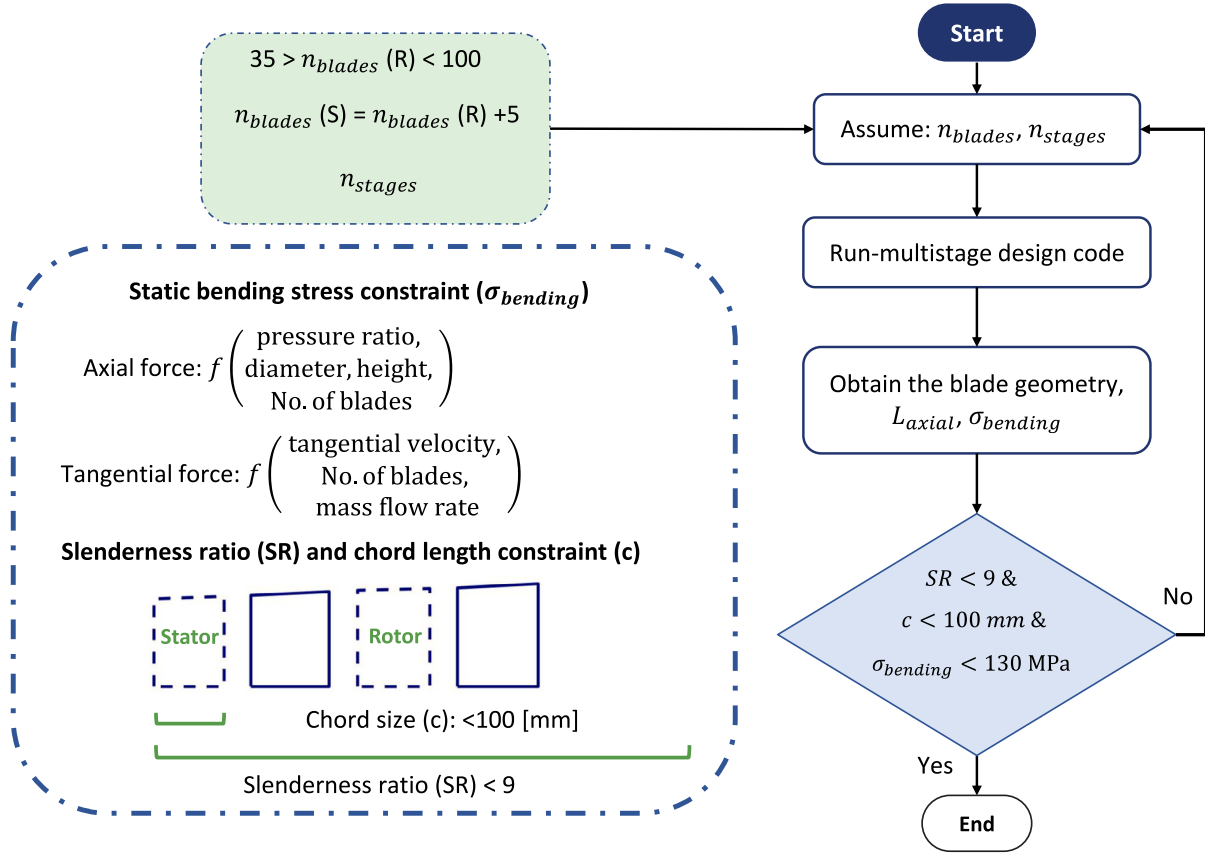$$\Lambda = \frac{\Delta h_0 - \frac{1}{2}C_2^2 + \frac{1}{2}C_3^2}{\Delta h_0} \tag{A.8}$$

Fig. A.17. Flow path optimisation methodology considering mechanical and rotordynamic design criteria.

hence,

$$\Delta h_0 (1 - \Lambda) = \frac{1}{2}C_2^2 - \frac{1}{2}C_3^2 \qquad (A.9)$$

Using Equations (A.6)–(A.7), this can be expressed as:

$$\Delta h_0 (1 - \Lambda) = \frac{1}{2}\left(C_a^2 + C_{w2}^2\right) - \frac{1}{2}\left(C_a^2 + C_{w3}^2\right) \qquad (A.10)$$

The tangential velocity component at the rotor outlet can then be obtained from:

$$C_{w3} = \sqrt{C_{w2}^2 - 2\Delta h_o (1 - \Lambda)} \qquad (A.11)$$

The enthalpy drop across the stages is defined as:

$$\Delta h_0 = U_2 C_{w2} + U_3 C_{w3} \qquad (A.12)$$

Substituting Equation (A.11) in the definition of the angular momentum (Equation (A.12)) enables calculating the tangential velocity components at the inlet and outlet of the rotor blades (C_{w2} & C_{w3}). Therefore, the flow angles can be obtained as follows:

$$\alpha_3 = \tan^{-1}\frac{C_{w3}}{Ca} \qquad (A.13)$$

$$\alpha_2 = \tan^{-1}\frac{C_{w2}}{Ca} \qquad (A.14)$$

$$\beta_2 = \tan^{-1}\left[\tan \alpha_2 - U_2/Ca\right] \qquad (A.15)$$

$$\beta_3 = \tan^{-1}\left[\tan \alpha_3 + U_3/Ca\right] \qquad (A.16)$$

Following this, velocities at the inlet and the outlet of the stator and rotor blade rows can be calculated (Equations (A.17)–(A.20)) and deviation angles can be obtained using the approach described by Ainley and Mathieson [57].

$$C_2 = \frac{C_a}{\cos \alpha_2} \qquad (A.17)$$

$$w_2 = \frac{C_a}{\cos \beta_2} \qquad (A.18)$$

$$C_3 = \frac{C_a}{\cos \alpha_3} \qquad (A.19)$$

$$w_3 = \frac{C_a}{\cos \beta_3} \qquad (A.20)$$

With the velocities fully defined, the thermophysical properties at the different turbine stations can be obtained through the equation of state:

$$[P, T] = f(h, s) \qquad (A.21)$$

$$[\rho, c_p, k] = f(P, T) \qquad (A.22)$$

At this stage, the flow areas can be obtained as a function of the density and the axial velocity, which is assumed to be constant across all the design stages. Following this, the hub diameter, mean diameter and diffusion angle can be calculated and U_3 can be updated. The process can then be reiterated until convergence. For the subsequent stages after the first stage, the axial velocity and enthalpy drop across the stage are known from the earlier stage and hence the process is initiated with the assumed degree of reaction, blade velocity U_2 and ratio $R = U_2/U_3$.

The aerodynamic performance of the turbine stage should be evaluated to predict the total-to-total turbine efficiency as defined in Eq. (A.23):

$$\eta_{tt} = \left[1 + \left(\frac{\zeta_R w_3^3 + \zeta_S C_2^2 \frac{T_3}{T_2}}{2(h_{01} - h_{03})}\right)\right]^{-1} \qquad (A.23)$$

where C and w are the absolute and relative velocities and ζ_S and ζ_R are the enthalpy loss coefficients for the stator and rotor respectively.

Table A.7

Verification results of the Loss models versus the experimental data and CFD simulations for the 140 kW air turbine [53].

Parameter	Symbol	Mean-line model [53]	EXP. Data [61–63]	CFD [64]
Stator outlet absolute flow angle [°C]	α_2	69.53	69.84	68.45
Stator outlet relative flow angle [°C]	β_2	6.58	7.13	4.82
Stator outlet absolute velocity [m/s]	C_2	156.78	170.8	153.84
Absolute Mach at Stator outlet [–]	M_2	0.42	0.457	0.412
Static pressure at Stator outlet [bar]	P_2	1.10	1.111	1.108
Static temperature at Stator inlet [K]	T_2	357.15	357.4	357.4
Static temperature at Stator outlet [K]	T_3	346.45	347.17	347.06
Rotor outlet relative flow angle [°C]	β_3	68.79	68.75	67.07
Rotor outlet absolute flow angle [°C]	α_3	0.73	2.45	7.58
Rotor outlet relative velocity [m/s]	W_3	151.53	166.3	157.51
Static pressure at rotor outlet [bar]	P_3	0.98	0.994	0.983
Static temperature at rotor outlet [K]	T_3	336.52	337.86	336.60
Stator mean radius [mm]	r_{2m}	186.42	181.5	181.5
Rotor mean radius [mm]	r_{3m}	186.42	185	185
Stator inlet blade height [mm]	h_1	88.1	89.2	89.2
Stator outlet (rotor inlet) blade height [mm]	h_2	95.79	97	97
Rotor outlet blade height [mm]	h_3	103.91	103	103
Number of Stator blades [–]	n_N	28	29	29
Number of rotor blades [–]	n_R	30	30	30
Stator loss coefficient [%]	ζ_S	6.2	3.79	5.82
Rotor loss coefficient [%]	ζ_R	7.5	9.08	6.66
Total-to-total stage efficiency [%]	η_{tt}	92.83	91.62	93.32

Table A.8

Verification results of the axial turbine design for air and sCO$_2$ and ORC turbines [53].

Parameter	Description	Mean-line model [53]	Literature results [23,61,62,65]
140 kW air turbine			
ζ_S (%)	Nozzle kinetic energy loss coefficient	0.062	0.038
ζ_R (%)	Rotor kinetic energy loss coefficient	0.074	0.091
η_{t_t} (%)	Total-to-total efficiency	0.928	0.916
Difference (%)	η_{tt}(%) with respect to Exp.Data	1.310	–
10 MW sCO$_2$ turbine/ [1st turbine stage]			
ζ_S(%)	Nozzle kinetic energy loss coefficient	0.037	–
ζ_R(%)	Rotor kinetic energy loss coefficient	0.072	–
η_{t_t} (%)	Total-to-total turbine efficiency	0.920	0.916
Difference (%)	η_{tt}(%) with respect to Exp.Data	0.437	–
440 kW ORC turbine			
Y_T	Total loss	0.183	0.180
η_{t_s}(%)	Total-to-static efficiency	0.896	0.891
Difference (%)	η_{ts}(%) with respect to Exp.Data	0.561	–
1520 kW ORC turbine			
Y_T	Total loss	0.446	0.444
η_{ts} (%)	Total-to-static efficiency	0.865	0.855
Difference (%)	η_{ts}(%) with respect to Exp.Data	1.169	–

Within the mean-line design context, losses are introduced in the form of stagnation pressure loss coefficients for the stator and rotor. These are defined as follows:

$$Y_S = \frac{p_{01} - p_{02}}{p_{02} - p_2} \tag{A.24}$$

$$Y_R = \frac{p_{03,rel} - p_{03,rel}}{p_{03,rel} - p_{3,rel}} \tag{A.25}$$

To calculate the total-to-total turbine efficiency (η_{tt}), the stator and rotor pressure loss coefficients ($Y_S \& Y_R$) are converted to enthalpy loss coefficients using the expressions:

$$\zeta_R = Y_R \times \left(1 + 0.5(k\ M_3^2)\right) \tag{A.26}$$

$$\zeta_S = Y_S \times \left(1 + 0.5(k\ M_2^2)\right) \tag{A.27}$$

where k is the specific heat ratio, and M_2 and M_3 are the absolute rotor inlet and relative rotor outlet Mach numbers respectively. Stagnation pressure loss coefficients for the stator and rotor ($Y_S \& Y_R$) are obtained by quantifying the energy losses that the working fluid experiences during the expansion in the stator and rotor blade rows using the Aungier loss model [54]. The design process can be summarised into the following steps and using the flow chart in Fig. A.16.

1. Assume ϕ, ψ, λ for the first design stage.
2. Define t/o, s/c, t_{cl}, k$_s$.
3. Assume the number of rotor blades (n_{blades}), number of stages (n_{stages}).
4. Assume the total-to-total turbine efficiency (η_{tt}), stator loss coefficients (ζ_S) and $R = U_2/U_3$.
5. Calcualte blade angles and velocity triangles.
6. Obtain flow thermodynamic properties, including pressure (P), temperature (T), density (ρ), speed of sound, the ratio of specific heats (k) and viscosity (ν), using Simulis [66].
7. Obtain detailed blade geometry, including, blade heights, annulus area, chord and axial chord length, blade pitch and throat-to-pitch ratio (o/c).
8. Estimate annulus losses and hence stage and turbine efficiency.
9. Obtain R and U_2 and re-iterate until the residual error between the assumed and calculated values satisfies the specified criteria.
10. Obtain turbine efficiency (η_{tt}) and re-iterate until the residual error between the assumed and calculated efficiency satisfies the specified criteria.
11. Calculate the tensile centrifugal and gas bending stresses on the turbine blades.

The designs are then evaluated from both the rotordynamic and mechanical perspective to ensure that $\sigma_{bending}$, c and SR are within the threshold limits. If the design does not meet the specified criteria, then the number of blades ($35 < n_{blades} < 100$) and the number of stages should be modified manually until the mechanical and rotordynamic design constraints are met (Fig. A.17); for example, the chord length should be increased, and the number of blades decreased accordingly to maintain the solidity, in order to reduce the bending stresses. The number of stages should also be reduced to bring the slenderness ratio within the specified limit.

The turbine design model has previously been verified against cases from the literature operating with conventional working fluids, such as air, and non-conventional working fluids including sCO_2. The design tool has been verified for a 140 kW air, 10 MW sCO_2 and 440 & 1520 kW organic Rankine cycle (ORC) to ensure the suitability of the design tool for different working fluids. The results of both verification cases were reported in the authors previous work [53], but a summary of the results is shown in Tables A.7 & A.8. Ultimately, a good agreement is obtained for both the geometric parameters as well as the total-to-total efficiency. Specifically, for the four selected verification cases the maximum percentage differences in the total-to-total and total-to-static efficiency were 1.3% and 1.2% respectively.

Appendix B. Candidate boundary conditions for turbine design

This annex presents the entire set of specifications employed in the turbine mean line design. More information regarding the selection criteria are provided in Section 4.1. A graphical representation of the different operating conditions considered is provided in Figs. B.18 to B.20, employing the same surface and contour plots previously discussed in Section 4.1 (Figs. 3 to 5). Optimum cases (font in bold in tables) are represented by star markers, and the remainder by circles.

(a) TIT=550ºC.   (b) TIT=700ºC

Fig. B.18. Thermal efficiency of a simple recuperated cycle operated with $CO_2/TiCl_4$ blends as a function of maximum cycle pressure and dopant molar fraction. Two turbines inlet temperatures are considered. The operating conditions employed in turbine design as identified by markers, the different Cases by black solid lines.
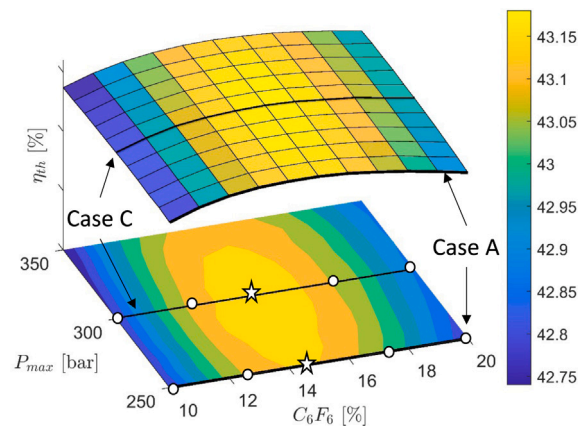
Fig. B.19. Thermal efficiency of a precompression cycle operated with CO_2/C_6F_6 blends as a function of maximum cycle pressure and dopant molar fraction, considering a turbine inlet temperature of 550 °C (results at 700 °C are not reported due to the limited thermal stability of this blend). The operating conditions employed in turbine design as identified by markers, the different Cases by black solid lines.
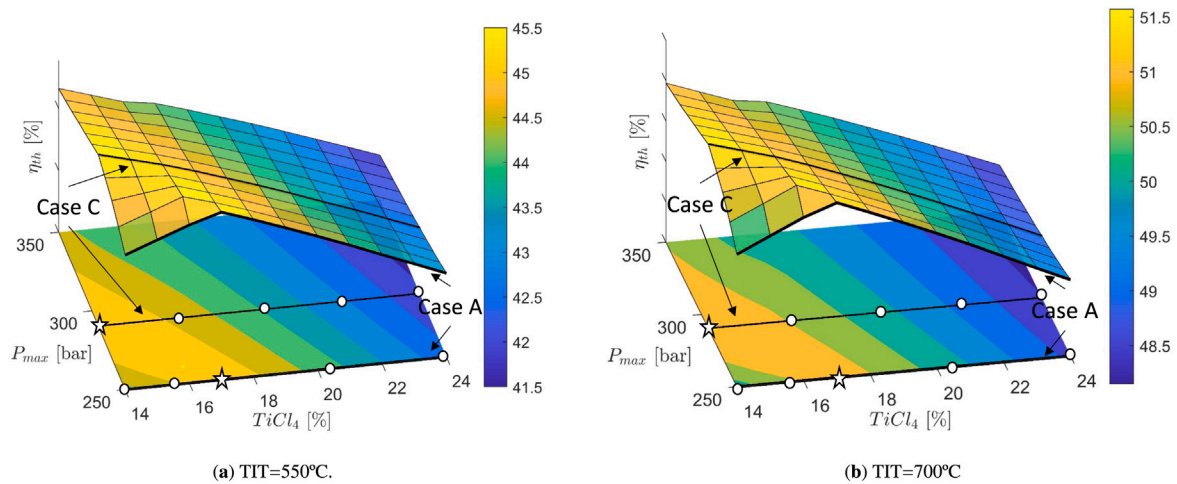
(**a**) TIT=550ºC.

(**b**) TIT=700ºC.

Fig. B.20. Thermal efficiency of a recompression cycle operated with sCO$_2$/SO$_2$ blends as a function of maximum cycle pressure and dopant molar fraction. Two turbines inlet temperatures are considered. The operating conditions employed in turbine design as identified by markers, the different Cases by black solid lines.
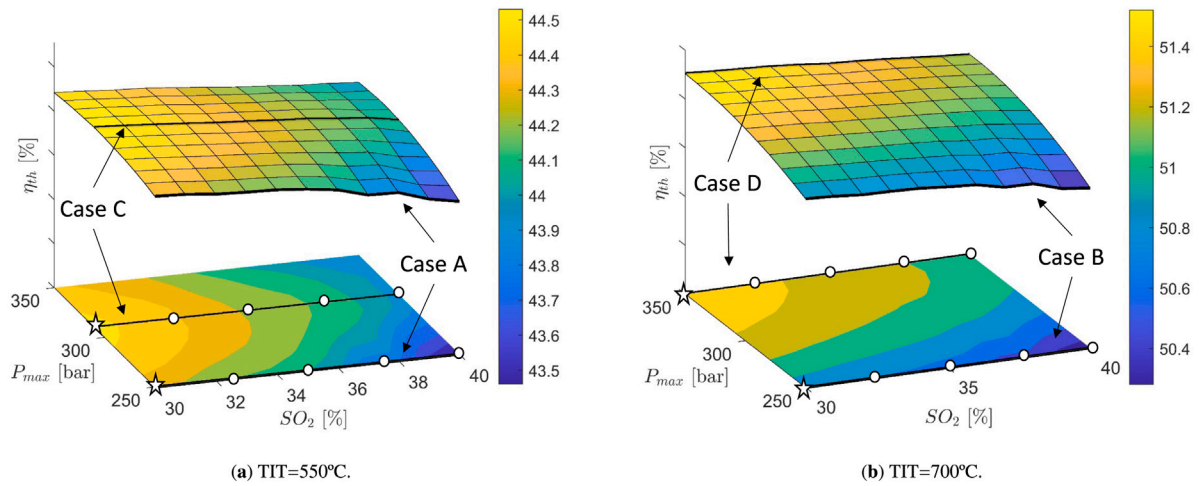
Table B.9
Complete set of specifications employed for turbine design (Cases A and B). The results for precompression cycle with CO$_2$/C$_6$F$_6$ at 700 °C are not reported due to the limited thermal stability of this blend.

		Case A (TIT = 550 °C, Pmax = 250 bar)					Case B (TIT = 700 °C, Pmax = 250 bar)				
CO$_2$/TiCl$_4$	Thermal Efficiency [%]	44.35	44.92	**45.42**	44.13	42.71	50.28	50.84	**51.33**	50.21	48.89
	TiCl$_4$ molar fraction [%]	14	15.5	**17**	20.5	24	14	15.5	**17**	20.5	24
	Turbine mass flow [kg/s]	1485	1535	**1577**	1677	1756	1174	1210	**1241**	1312	1367
	Turbine Inlet T [°C]	550	550	**550**	550	550	700	700	**700**	700	700
	Turbine Inlet P [bar]	242.6	242.6	**242.6**	242.6	242.6	242.6	242.6	**242.6**	242.6	242.6
	Turbine Outlet P [bar]	98.13	97.66	**97.14**	95.40	93.44	98.13	97.66	**97.14**	95.40	93.44
	Total turbine isentropic enthalpy drop [kJ/kg]	90.36	87.65	**85.14**	80.24	76.08	109.80	106.68	**103.80**	98.25	93.59
	Total-to-total turbine efficiency [%]	92.92	93.00	**92.50**	92.65	92.05	93.52	93.24	**93.29**	93.01	93.10
CO$_2$/C$_6$F$_6$	Thermal Efficiency [%]	42.81	43.12	**43.17**	43.08	42.87	–	–	–	–	–
	C$_6$F$_6$ molar fraction [%]	10	12.5	**14.5**	17.5	20	–	–	–	–	–
	Turbine mass flow [kg/s]	1098	1129	**1152**	1186	1212	–	–	–	–	–
	Turbine Inlet T [°C]	550	550	**550**	550	550	–	–	–	–	–
	Turbine Inlet P [bar]	238.9	238.9	**238.9**	238.9	238.9	–	–	–	–	–
	Turbine Outlet P [bar]	64.63	62.33	**61.48**	58.81	57.53	–	–	–	–	–
	Total turbine isentropic enthalpy drop [kJ/kg]	143.38	139.01	**134.47**	130.29	125.94	–	–	–	–	–
	Total-to-total turbine efficiency [%]	93.84	93.64	**93.68**	93.46	93.49	–	–	–	–	–
sCO$_2$/SO$_2$	Thermal Efficiency [%]	**44.32**	44.21	44.11	43.82	43.46	**50.87**	50.79	50.71	50.54	50.28
	SO$_2$ molar fraction [%]	**30**	32.5	35	37.5	40	**30**	32.5	35	37.5	40
	Turbine mass flow [kg/s]	**1016**	999.9	991.3	995.6	1004	**780.8**	772.8	760.4	760.0	761.8
	Turbine Inlet T [°C]	**550**	550	550	550	550	**700**	700	700	700	700
	Turbine Inlet P [bar]	**238.9**	238.9	238.9	238.9	238.9	**238.9**	238.9	238.9	238.9	238.9
	Turbine Outlet P [bar]	**69.93**	67.75	65.60	63.47	61.35	**69.93**	67.75	65.60	63.47	61.35
	Total turbine isentropic enthalpy drop [kJ/kg]	**151.87**	153.53	155.18	156.84	158.51	**184.14**	186.32	188.50	190.70	192.92
	Total-to-total turbine efficiency [%]	**94.07**	94.04	94.02	94.03	94.03	**94.03**	94.00	93.96	93.95	93.95

Table B.10

Complete set of specifications employed for turbine design (Cases C and D). The results for precompression cycle with CO_2/C_6F_6 at 700 °C are not reported due to the limited thermal stability of this blend.

		Case C (TIT = 550 °C, Pmax = Popt)					Case D (TIT = 700 °C, Pmax = Popt)				
$CO_2/TiCl_4$	Thermal Efficiency [%]	**45.55**	44.86	44.02	43.09	42.13	**51.57**	50.96	50.21	49.97	48.53
	$TiCl_4$ molar fraction [%]	**14**	16.5	19	21.5	24	**14**	16.5	19	21.5	24
	Turbine mass flow [kg/s]	**1316**	1387	1455	1521	1571	**1032**	1084	1132	1178	1212
	Turbine Inlet T [°C]	**550**	550	550	550	550	**700**	700	700	700	700
	Turbine Inlet P [bar]	**281.4**	281.4	281.4	281.4	281.4	**281.4**	281.4	281.4	281.4	281.4
	Turbine Outlet P [bar]	**98.13**	97.33	96.22	94.79	93.44	**98.13**	97.33	96.22	94.79	93.44
	Total turbine isentropic enthalpy drop [kJ/kg]	**104.07**	98.84	94.36	90.52	86.93	**126.80**	120.79	115.67	111.33	107.30
	Total-to-total turbine efficiency [%]	**92.94**	93.07	92.77	92.38	92.48	**93.53**	93.39	93.47	93.27	93.03
CO_2/C_6F_6	Thermal Efficiency [%]	42.80	43.10	**43.17**	43.07	42.89	–	–	–	–	–
	C_6F_6 molar fraction [%]	10	12.5	**15**	17.5	20	–	–	–	–	–
	Turbine mass flow [kg/s]	987.7	1016	**1046**	1073	1101	–	–	–	–	–
	Turbine Inlet T [°C]	550	550	**550**	550	550	–	–	–	–	–
	Turbine Inlet P [bar]	286.7	286.7	**286.7**	286.7	286.7	–	–	–	–	–
	Turbine Outlet P [bar]	66.13	64.28	**63.47**	60.68	58.91	–	–	–	–	–
	Total turbine isentropic enthalpy drop [kJ/kg]	159.57	153.64	**146.93**	143.49	139.15	–	–	–	–	-
	Total-to-total turbine efficiency [%]	93.55	93.58	**93.42**	93.45	93.49	–	–	–	–	-
CO_2/SO_2	Thermal Efficiency [%]	**44.53**	44.42	44.29	44.16	43.95	**51.52**	51.44	51.31	51.23	51.1
	SO_2 molar fraction [%]	**30**	32.5	35	37.5	40	**30**	32.5	35	37.5	40
	Turbine mass flow [kg/s]	**907.8**	903.0	892.0	888.8	879.9	**649.7**	645.9	639.2	636.2	634.7
	Turbine Inlet T [°C]	**550**	550	550	550	550	**700**	700	700	700	700
	Turbine Inlet P [bar]	**296.3**	296.3	296.3	296.3	296.3	**334.5**	334.5	334.5	334.5	334.5
	Turbine Outlet P [bar]	**69.93**	67.75	65.60	63.47	61.35	**69.93**	67.75	65.60	63.47	61.35
	Total turbine isentropic enthalpy drop [kJ/kg]	**175.15**	176.34	177.53	178.73	179.95	**229.37**	230.77	232.17	233.60	235.06
	Total-to-total turbine efficiency [%]	**93.67**	93.84	93.82	93.82	93.80	**93.50**	93.50	93.47	93.61	93.61

References

[1] S. Besarati, D. Goswami, Chapter8 - Supercritical CO_2 and other advanced power cycles for concentrating solar thermal (CST) systems, in: M.J. Blanco, L.R. Santigosa (Eds.), Advances in Concentrating Solar Thermal Research and Technology, in: Woodhead Publishing Series in Energy, Woodhead Publishing, 2017, pp. 157–178, http://dx.doi.org/10.1016/B978-0-08-100516-3.00008-3.

[2] F. Crespi, D. Sánchez, G.S. Martínez, T. Sánchez-Lencero, F. Jiménez-Espadafor, Potential of supercritical carbon dioxide power cycles to reduce the levelised cost of electricity of contemporary concentrated solar power plants, Appl. Sci. 10 (15) (2020) 5049, http://dx.doi.org/10.3390/app10155049.

[3] F. Crespi, P.R. de Arriba, D. Sánchez, A. Ayub, G. Di Marcoberardino, C. Invernizzi, G. Martínez, P. Iora, D. Di Bona, M. Binotti, et al., Thermal efficiency gains enabled by using CO_2 mixtures in supercritical power cycles, Energy 238 (2022) 121899, http://dx.doi.org/10.1016/j.energy.2021.121899.

[4] M.T. White, G. Bianchi, L. Chai, S.A. Tassou, A.I. Sayma, Review of supercritical CO_2 technologies and systems for power generation, Appl. Therm. Eng. 185 (2021) 116447, http://dx.doi.org/10.1016/j.applthermaleng.2020.116447.

[5] Z. Ma, C.S. Turchi, Advanced Supercritical Carbon Dioxide Power Cycle Configurations for Use in Concentrating Solar Power Systems, National Renewable Energy Lab. (NREL), Golden, CO (United States), 2011.

[6] O.A. Aqel, M.T. White, M. Khader, A. Sayma, Sensitivity of transcritical cycle and turbine design to dopant fraction in CO_2-based working fluids, Appl. Therm. Eng. 190 (2021) 116796, http://dx.doi.org/10.1016/j.applthermaleng.2021.116796.

[7] M. Binotti, G. Manzolini, Supercritical carbon dioxide/alternative fluids blends for efficiency upgrade of solar power plant, in: 3rd Euroepan Supercritical CO_2 Conference, DEU, 2019, pp. 141–149.

[8] G. Manzolini, M. Binotti, D. Bonalumi, C. Invernizzi, P. Iora, CO_2 mixtures as innovative working fluid in power cycles applied to solar plants. Techno-economic assessment, Sol. Energy 181 (2019) 530–544, http://dx.doi.org/10.1016/j.solener.2019.01.015.

[9] SCARABEUS project, 2019, https://www.scarabeusproject.eu/.

[10] D. Bonalumi, S. Lasala, E. Macchi, CO_2-TiCl$_4$ working fluid for high-temperature heat source power cycles and solar application, Renew. Energy 147 (2020) 2842–2854, http://dx.doi.org/10.1016/j.renene.2018.10.018.

[11] G. Manzolini, M. Binotti, E. Morosini, D. Sánchez, F. Crespi, G. Di Marcober-ardino, P. Iora, C. Invernizzi, Adoption of CO_2 blended with C_6F_6 as working fluid in CSP plants, in: AIP Conference Proceedings, Vol. 2445, No. 1, AIP Publishing LLC, 2022, 090005, http://dx.doi.org/10.1063/5.0086520.

[12] F. Crespi, P.R. de Arriba, D. Sánchez, A. Muñoz, Preliminary investigation on the adoption of CO_2-SO$_2$ working mixtures in a transcritical recompression cycle, Appl. Therm. Eng. 211 (2022) 118384, http://dx.doi.org/10.1016/j.applthermaleng.2022.118384.

[13] C. Turchi, Z. Ma, T. Neises, M. Wagner, Thermodynamic study of advanced supercritical carbon dioxide power cycles for concentrating solar power systems, J. Sol. Energy Eng. 135 (4) (2013).

[14] F. Crespi, D. Sánchez, T. Sánchez, G. Martínez, Capital cost assessment of concentrated solar power plants based on supercritical carbon dioxide power cycles, J. Eng. Gas Turbines Power 141 (7) (2019) http://dx.doi.org/10.1115/1.4042304.

[15] Y. Ahn, S.J. Bae, M. Kim, S.K. Cho, S. Baik, J.I. Lee, J.E. Cha, Review of supercritical CO_2 power cycle technology and current status of research and development, Nucl. Eng. Technol. 47 (6) (2015) 647–661, http://dx.doi.org/10.1016/j.net.2015.06.009.

[16] S.I. Salah, M.A. Khader, M.T. White, A.I. Sayma, Mean-line design of a super-critical CO_2 micro axial turbine, Appl. Sci. 10 (15) (2020) https://www.mdpi.com/2076-3417/10/15/5069.

[17] J. Qi, T. Reddell, K. Qin, K. Hooman, I.H.J. Jahn, Supercritical CO_2 Radial Turbine Design Performance as a Function of Turbine Size Parameters, J. Turbomach. 139 (8) (2017).

[18] N. Holaind, G. Bianchi, M. De Miol, S.S. Saravi, S.A. Tassou, A. Leroux, H. Jouhara, Design of radial turbomachinery for supercritical CO_2 systems using theoretical and numerical CFD methodologies, Energy Procedia 123 (2017) 313–320, http://dx.doi.org/10.1016/j.egypro.2017.07.256.

[19] A. Zhou, J. Song, X. Li, X. Ren, C. Gu, Aerodynamic design and numerical analysis of a radial inflow turbine for the supercritical carbon dioxide Brayton cycle, Appl. Therm. Eng. 132 (2018) 245–255, http://dx.doi.org/10.1016/j.applthermaleng.2017.12.106.

[20] H. Zhang, H. Zhao, Q. Deng, Z. Feng, Aerothermodynamic design and numerical investigation of supercritical carbon dioxide turbine, in: Proceedings of the ASME Turbo Expo: Turbine Technical Conference and Exposition, June 15–19, Montreal, Quebec, Canada, 2015, http://dx.doi.org/10.1115/GT2015-42619.

[21] D. Luo, Y. Liu, X. Sun, D. Huang, The design and analysis of supercritical carbon dioxide centrifugal turbine, Appl. Therm. Eng. 127 (2017) 527–535, http://dx.doi.org/10.1016/j.applthermaleng.2017.08.039.

[22] J. Lee, J.I. Lee, Y. Ahn, H. Yoon, Design methodology of supercritical CO_2 Brayton cycle turbomachineries, in: Proceedings of the ASME Turbo Expo: Turbine Technical Conference and Exposition, June 11–15, Copenhagen, Denmark, 2012, http://dx.doi.org/10.1115/GT2012-68933.

[23] D. Shi, L. Zhang, Y. Xie, D. Zhang, Aerodynamic design and off-design performance analysis of a multi-stage S-CO$_2$ axial turbine based on solar power generation system, Appl. Sci. 9 (2019) 714, http://dx.doi.org/10.3390/app9040714.

[24] J. Schmitt, R. Willis, D. Amos, J. Kapat, C. Custer, Study of a supercritical CO_2 turbine with TIT of 1350 K for brayton cycle with 100 MW class output: Aerodynamic analysis of stage 1 vane, in: Proceedings of the ASME Turbo Expo, 2014, http://dx.doi.org/10.1115/GT2014-27214.

[25] V. Dostal, M. Driscoll, P. Hejzlar, in: V. Dostal, M. Driscoll, P. Hejzlar (Eds.), A Supercritical Carbon Dioxide Cycle for Next Generation Nuclear Reactors, Thesis MIT-ANP-TR-100, Massachusetts Institute of Technology, Boston, MA, 2004.

[26] R. Bidkar, G. Musgrove, M. Day, C. Kulhanek, T. Allison, Conceptual designs of 50 MW_e and 450 MW_e supercritical CO_2 turbomachinery trains for power generation from coal. Part 2: Compressors, in: 5th Int. Symp. - Supercrit. CO_2 Power Cycles March 28-31, 2016, San Antonio, Texas, 2016, pp. 1–18.

[27] T. Allison, J. Moore, R. Pelton, J. Wilkes, B. Ertas, 7 - turbomachinery, in: K. Brun, P. Friedman, R. Dennis (Eds.), Fundamentals and Applications of Supercritical Carbon Dioxide (SCO₂) Based Power Cycles, Woodhead Publishing, 2017, pp. 147–215, http://dx.doi.org/10.1016/B978-0-08-100804-1.00007-4.

[28] E.M. Clementoni, T.L. Cox, M.A. King, Off-Nominal Component Performance in a Supercritical Carbon Dioxide Brayton Cycle, J. Eng. Gas Turbines Power 138 (1) (2015) http://dx.doi.org/10.1115/1.4031182.

[29] M. Utamura, H. Hasuike, K. Ogawa, T. Yamamoto, T. Fukushima, T. Watanabe, T. Himeno, Demonstration of Supercritical CO_2 Closed Regenerative Brayton Cycle in a Bench Scale Experiment, in: Proceedings of the ASME Turbo Expo: Turbine Technical Conference and Exposition, June 11–15, Copenhagen, Denmark, 2012, pp. 155–164, http://dx.doi.org/10.1115/GT2012-68697.

[30] S.A. Wright, R.F. Radel, M.E. Vernon, P.S. Pickard, G.E. Rochau, Operation and analysis of a super-critical CO_2 brayton cycle, 2010, http://dx.doi.org/10.2172/984129.

[31] K.J. Kimball, E.M. Clementoni, Supercritical carbon dioxide brayton power cycle development overview, in: Proceedings of the ASME Turbo Expo: Turbine Technical Conference and Exposition, June 11–15, Copenhagen, Denmark, 2012, pp. 931–940, http://dx.doi.org/10.1115/GT2012-68204.

[32] J. Cho, H. Shin, H.-S. Ra, G. Lee, C. Roh, B. Lee, Y.-J. Baik, Development of the supercritical carbon dioxide power cycle experimental loop in KIER, 2016, http://dx.doi.org/10.1115/GT2016-57460.

[33] J. Moore, K. Brun, N. Evans, C. Kalra, Development of 1 MW_e Supercritical CO_2 Test Loop, in: Proceedings of ASME Turbomachinery Technical Conference and Exposition, June 15–19, Montreal, Quebec, Canada, 2015, http://dx.doi.org/10.1115/GT2015-43771.

[34] N. Weiland, R. Dennis, R. Ames, S. Lawson, P. Strakey, Chapter 12 - fossil energy, in: K. Brun, P. Friedman, R. Dennis (Eds.), Fundamentals and Applications of Supercritical Carbon Dioxide (sCO₂) Based Power Cycles, Woodhead Publishing, 2017, pp. 293–338, http://dx.doi.org/10.1016/B978-0-08-100804-1.00012-8.

[35] C. Kalra, D. Hofer, E. Sevincer, J. Moore, K. Brun, Development of high efficiency hot gas turbo-expander for optimized CSP supercritical CO_2 power block operation, in: The Fourth International Symposium—Supercritical CO_2 Power Cycles (SCO₂), Citeseer, 2014, pp. 1–11.

[36] NFPA 704: Standard system for the identification of the hazards of materials for emergency response, 2022, URL https://www.nfpa.org/codes-and-standards/all-codes-and-standards/list-of-codes-and-standards/detail?code=704. (Online, Accessed 6 February 2022).

[37] Thermoflow inc, thermoflow suite - thermoflex software, 2022, URL https://www.thermoflow.com/products_generalpurpose.html. (Online, Accessed 6 February 2022).

[38] F. Crespi, P. Rodríguez de Arriba, D. Sánchez, A. Muñoz, T. Sánchez, The potential of supercritical cycles based on CO_2 mixtures in concentrated solar power plants: an exergy-based analysis, in: Proceedings of the 6th International Seminar on ORC Power Systems, 2021, http://dx.doi.org/10.14459/2021mp1633114.

[39] W.C. Reynolds, P. Colonna, Thermodynamics: Fundamentals and Engineering Applications, Cambridge University Press, 2018, http://dx.doi.org/10.1017/9781139050616.

[40] C. Invernizzi, Closed power cycles, in: Lecture Notes in Energy, Vol. 11, Springer, 2013, http://dx.doi.org/10.1007/978-1-4471-5140-1.

[41] List of ozone-depleting substances by US environmental protection agency, 2023, URL https://www.epa.gov/ozone-layer-protection/ozone-depleting-substances. (Online, Accessed 14 February 2023).

[42] Overview of greenhouse gases by US environmental protection agency, 2023, URL https://www.epa.gov/ghgemissions/overview-greenhouse-gases. (Online, Accessed 14 February 2023).

[43] SO₂ pollution effects by US environmental protection agency, 2023, URL https://www.epa.gov/so2-pollution/sulfur-dioxide-basics#effects. (Online, Accessed 14 February 2023).

[44] X. Liao, S. Chalumeau, F. Crespi, C. Prieto, A. Lopez-Roman, P. Rodriguez de Arriba, N. Martínez, D. Sánchez, A. Paggini, P. David, Life cycle assessment of innovative concentrated solar power plants using supercritical carbon dioxide mixtures, in: Proceedings of ASME Turbo Expo 2022: Turbomachinery Technical Conference and Exposition, June 13–17, Rotterdam, Netherlands, 2022.

[45] P. Rodríguez-deArriba, F. Crespi, D. Sánchez, A. Muñoz, T. Sánchez, The potential of transcritical cycles based on CO_2 mixtures: An exergy-based analysis, Renew. Energy 199 (2022) 1606–1628, http://dx.doi.org/10.1016/j.renene.2022.09.041.

[46] D. Kirk-Othmer, Encyclopedia of Chemical Technology, Vol. 23, fourth ed., Wiley Interscience Publication, 2001, http://dx.doi.org/10.1002/0471238961.

[47] G. Di Marcoberardino, E. Morosini, D. Di Bona, P. Chiesa, C. Invernizzi, P. Iora, G. Manzolini, Experimental characterisation of $CO_2+ C_6F_6$ mixture: Thermal stability and vapour liquid equilibrium test for its application in transcritical power cycle, Appl. Therm. Eng. 212 (2022) 118520, http://dx.doi.org/10.1016/j.applthermaleng.2022.118520.

[48] G. Angelino, Real Gas Effects in Carbon Dioxide Cycles, Vol. 79832, American Society of Mechanical Engineers, 1969, http://dx.doi.org/10.1115/69-GT-102.

[49] E. Morosini, A. Ayub, G. di Marcoberardino, C.M. Invernizzi, P. Iora, G. Manzolini, Adoption of the $CO_2+ SO_2$ mixture as working fluid for transcritical cycles: A thermodynamic assessment with optimized equation of state, Energy Convers. Manage. 255 (2022) 115263, http://dx.doi.org/10.1016/j.enconman.2022.115263.

[50] A.M. Dias, H. Carrier, J.L. Daridon, J.C. Pamies, L.F. Vega, J.A. Coutinho, I.M. Marrucho, Vapor- liquid equilibrium of carbon dioxide- perfluoroalkane mixtures: experimental data and SAFT modeling, Ind. Eng. Chem. Res. 45 (7) (2006) 2341–2350.

[51] W. Tolley, R. Izatt, J. Oscarson, Titanium tetrachloride-supercritical carbon dioxide interaction: A solvent extraction and thermodynamic study, Metall. Trans. B 23 (1) (1992) 65–72.

[52] C. Coquelet, A. Valtz, P. Arpentinier, Thermodynamic study of binary and ternary systems containing CO_2+ impurities in the context of CO_2 transportation, Fluid Phase Equilib. 382 (2014) 205–211, http://dx.doi.org/10.1016/j.fluid.2014.08.031.

[53] S.I. Salah, M.T. White, A.I. Sayma, A comparison of axial turbine loss models for air, sCO₂ and ORC turbines across a range of scales, Int. J. Thermofluids (2022) 100156, http://dx.doi.org/10.1016/j.ijft.2022.100156.

[54] R.H. Aungier, Turbine Aerodynamics: Axial-Flow and Radial-Flow Turbine Design and Analysis, ASME Press, 2006, http://dx.doi.org/10.1115/1.802418.

[55] S.F. Smith, A simple correlation of turbine efficiency, J. Royal Aeronaut. Soc. 69 (655) (1965) 467–470, http://dx.doi.org/10.1017/S0001924000059108.

[56] S.C. Kacker, U. Okapuu, A mean line prediction method for axial flow turbine efficiency, J. Eng. Power 104 (1) (1982) 111–119, http://dx.doi.org/10.1115/1.3227240.

[57] D. Ainley, G.C. Mathieson, A Method of Performance Estimation for Axial-Flow Turbines, Tech. Rep., Aeronautical Research Council, 1951.

[58] S. Dixon, C. Hall, Chapter 4 - Axial-flow turbines: mean-line analysis and design, in: S. Dixon, C. Hall (Eds.), Fluid Mechanics and Thermodynamics of Turbomachinery, sixth ed., Butterworth-Heinemann, Boston, 2010, pp. 97–141, http://dx.doi.org/10.1016/B978-1-85617-793-1.00004-3.

[59] S.I. Salah, Design and Analysis of Supercritical Carbon-Dixoide Axial Turbines (Ph.D. thesis), City University London, 2023.

[60] A.S. Abdeldayem, S.I. Salah, O. Aqel, M.T. White, A.I. Sayma, Design of a 130 MW axial turbine operating with a supercritical carbon dioxide mixture for the scarabeus project, in: 15th European Turbo-machinery conference, 24-28th April, Budapest, Hungry, 2023, http://dx.doi.org/10.1115/GT2015-42619.

[61] G. Groschup, Strömungstechnische Untersuchung einer Axialturbinenstufe im Vergleich Zum Verhalten Der Ebenen Gitter Ihrer Beschaufelung, 1977.

[62] C. Hirsch, J. Denton, Through Flow Calculations in Axial Turbomachines, AGARD Advisory Report N.175; Technical Report, AGARD, Propulsion and Energetics Panel, Working Group 12, Neuilly Sur Seine, France, 1981.

[63] P. Kötzing, B. Evers, Test Case e/tu-4, 4-Stage Low Speed Turbine, AGARD Report No.275 AR-275; Technical Report; AGARD, Neuilly Sur Seine, France, 1990.

[64] A. Meroni, A. La Seta, J.G. Andreasen, L. Pierobon, G. Persico, F. Haglind, Combined turbine and cycle optimization for organic Rankine cycle power systems—Part A: turbine model, Energies 9 (5) (2016) URL https://www.mdpi.com/1996-1073/9/5/313.

[65] L. Da Lio, G. Manente, A. Lazzaretto, New efficiency charts for the optimum design of axial flow turbines for organic Rankine cycles, Energy 77 (2014) 447–459, http://dx.doi.org/10.1016/j.energy.2014.09.029.

[66] Simulis thermodynamics, 2019, Available online: http://www.prosim.net/en/software-simulis-thermodynamics-mixture-properties-and-fluid-phase-equilibria-calculations-3.php.